AGU PUBLICATIONS

JGR

Journal of Geophysical Research: Atmospheres

RESEARCH ARTICLE
10.1002/2016JD025133

Key Points:
- Contrasting conditions in premonsoon and monsoon environments determine dynamical and microphysical characteristics of deep convection
- Uncertainty of the mixing type (homogeneous versus inhomogeneous) due to low-resolution observations
- Mixing in deep cumulus is a two-step process

Supporting Information:
- Supporting Information S1

Correspondence to:
S. Bera,
sbera.cat@tropmet.res.in

Citation:
Bera, S., T. V. Prabha, and W. W. Grabowski (2016), Observations of monsoon convective cloud microphysics over India and role of entrainment-mixing, *J. Geophys. Res. Atmos.*, *121*, 9767–9788, doi:10.1002/2016JD025133.

Received 23 MAR 2016
Accepted 26 JUL 2016
Accepted article online 29 JUL 2016
Published online 31 AUG 2016

Observations of monsoon convective cloud microphysics over India and role of entrainment-mixing

Sudarsan Bera[1], Thara V. Prabha[1], and Wojciech W. Grabowski[2]

[1]Indian Institute of Tropical Meteorology, Pune, India, [2]National Center for Atmospheric Research, Boulder, Colorado, USA

Abstract Microphysical characteristics of premonsoon and monsoon deep cumuli over India observed by an instrumented aircraft are contrasted focusing on influences of environmental conditions and entrainment-mixing processes. Differences in the lower tropospheric temperature and moisture profiles lead to contrasting undiluted cloud buoyancy profiles around the cloud base, larger in the premonsoon case. It is argued that this affects the variation of the mean and maximum cloud droplet number concentrations and the droplet radius within the lowest several hundred meters above the cloud base. The conserved-variable thermodynamic diagram analysis suggests that entrained parcels originate from levels close to the observational level. Mixing processes and their impact on the droplet size distribution (DSD) are investigated contrasting 1 Hz and 10 Hz observations. Inhomogeneous-type mixing, likely because of unresolved small-scale structures associated with active turbulent stirring, is noted at cloud edge volumes where dilution is significant and DSDs shift toward smaller sizes with reduced droplet number concentrations due to complete evaporation of smaller droplets and partial evaporation of larger droplets. DSDs within cloud core volumes suggest that the largest droplets are formed in the least diluted volumes where raindrops can form at higher levels; no superadiabatic droplet growth is observed. The typical diluted parcel size is approximately 100–200 m for cloud edge volumes, and it is much smaller, 10–20 m, for cloud core volumes. Time scale analysis indicates the possibility of inhomogeneous type mixing within the diluted cloud edge volumes at spatial scales of a 100 m or more.

1. Introduction

Cumulus clouds play an important role in hydrological cycle and radiative forcing of climate due to their significant contribution to the overall surface rainfall and cloud albedo [*Browning and Gurney*, 1999; *Grabowski and Petch*, 2009]. They are numerous and predominant over a variety of geographical settings like tropical and subtropical regions [*Norris*, 1998]. Deep cumulus clouds bring much rainfall in the tropics [*Gray and Jacobson*, 1977] and moisten the upper atmosphere [*Sherwood et al*., 2004]. Understanding the precipitation formation processes in these deep cumuli is important to reduce the uncertainty in the climate models [*Sherwood et al*., 2014].

One of key processes affecting cumulus convection is entrainment [e.g., *Romps*, 2016, and references therein]. Unsaturated cloud-free environmental air enters into growing cumulus through the lateral edges, mixes with the saturated air rising from cloud base [*Stommel*, 1947], and leads to a significant dilution of the cloud mass [*Warner*, 1955]. The entrainment of droplet free dry air into a cumulus cloud is driven by the instability of the cloud-environment interface [*Baker et al*., 1984; *Klaassen and Clark*, 1985]. A detailed study on the cloud-environment interface instability is provided in *Grabowski and Clark* [1991, 1993a, 1993b]. The instability involves large (i.e., comparable to the size of the cloud) entraining eddies that bring the environmental air into the cloud interior. These eddies break into smaller filaments until the mixture is homogenized at a scale close to the Kolmogorov microscale (order of 10^{-3} m) by the molecular diffusion [*Baker et al*., 1984; *Broadwell and Breidenthal*, 1982]. Due to continuous breaking of large eddies into smaller filaments, turbulent kinetic energy is transferred to smaller scale, and the latent heat is released at the dissipation scales [e.g., *Grabowski*, 1993].

In addition to the dilution of cloudy mass during the entrainment of cloud-free environmental air, the water vapor mixing ratio is modified if the entrained air is subsaturated and/or the environmental temperature is different from the one inside the cloud. At the end, the saturation equilibrium is restored by droplet evaporation. The evaporation of droplets due to entrainment and mixing in cumulus clouds affects the droplet size distribution (DSD) [e.g., *Jensen and Baker*, 1989; *Baker et al*., 1980; *Tölle and Krueger*, 2014]. For

the monodisperse DSD, the mixing can lead to the reduction of the droplet size with no change of the total number of droplets as in the homogeneous mixing [*Warner*, 1973], the reduction in the droplet total number and no change in droplet size as in the extremely inhomogeneous mixing [*Latham and Reed*, 1977; *Baker et al*., 1980], or reduction in both the droplet size and the droplet number as in the intermediate mixing [*Lu et al*., 2013]. Note that the droplet concentration does change in all types of mixing: droplets are dispersed over a larger volume in the case of the homogeneous mixing and some droplets evaporate in the extreme inhomogeneous mixing. With a spectrum of cloud droplets, the outcome of the mixing is more difficult to assess. For instance, homogeneous mixing can lead to either a shift of the droplet spectrum toward smaller sizes (and thus no change of the total droplet number) or it can result in partial evaporation of the droplet spectrum (i.e., complete evaporation of some droplets from the smallest droplet end of the spectrum). *Baker et al*. [1980] suggested that the time scale of turbulent mixing (τ_{mix}) and the time scale of droplet evaporation (τ_{evap}) determine the characteristics of the mixing process. *Lu et al*. [2014] studied scale dependence of entrainment-mixing process and found that mixing changes from homogeneous to inhomogeneous type with increasing mixing time scale.

In warm (i.e., ice-free) clouds, cloud droplet size distribution (DSD) is the key for rain initiation. DSD changes due to entrainment and mixing, a fundamental process in cumulus clouds, continue to be subject of a debate in the cloud physics community [e.g., *Jensen et al*., 1985; *Brenguier and Grabowski*, 1993; *Jarecka et al*., 2013; *Lu et al*., 2013]. Entraining environmental air through lateral cloud boundaries as plumes [*Stommel*, 1947] or blobs [*Scorer and Ludlam*, 1953] were the classical concepts of cumulus entrainment. Entrainment can also happen through the cloud top, and then the entrained air can penetrate inside the cumulus cloud [*Squires*, 1958]. Using conserved thermodynamic parameters, *Paluch* [1979] argued that cumulus entrainment involves two single layers, the cloud base, and the cloud top, while lateral entrainment is less significant. In contrast, the study of Montana shallow cumuli by *Blyth et al*. [1988] suggests that the source of entrained air is close to or slightly above the observational level. More recently, *Böing et al*. [2014] showed that entrainment in simulated deep cumulus is mainly through lateral cloud boundaries at many levels.

Subsequent mixing of entrained dry air with saturated cloudy volume dilutes the liquid water content of an adiabatic cloud and changes its microphysical structure. There seems to be a disagreement between the observed and modeled DSD spectral width [e.g., *Yum and Hudson*, 2005; *Brenguier and Chaumat*, 2001; *Jensen and Baker*, 1989]. Entrainment also introduces new cloud condensation nuclei (CCN) into the cloud from the environment. Entrained CCN can become activated and produce small droplets, hence modifying the spectral shape and size distribution [*Warner*, 1969; *Paluch and Knight*, 1984; *Brenguier and Grabowski*, 1993; *Su et al*., 1998; *Lasher-Trapp et al*., 2005]. Entrainment-related activation of fresh CCN away from the cloud base is referred to as the secondary activation [e.g., *Krueger et al*., 2006; *Lehmann et al*., 2009; *Prabha et al*., 2011]. Modeling study of *Slawinska et al*. [2012] showed evidences for in-cloud activation of fresh CCN above cloud base. Entrainment was also argued to produce superadiabatic droplets in diluted cloud parcels that experienced extremely inhomogeneous mixing (i.e., droplet concentration was reduced without changing the mean droplet radius) [*Korolev and Isaac*, 2000]. This is because higher supersaturations can be generated inside such parcels, and thus, droplet diffusional growth can be enhanced [e.g., *Paluch and Baumgardner*, 1989; *Korolev and Isaac*, 2000]. In addition, cloud dilution due to entrainment and mixing has important implications for radiative properties of clouds [e.g., *Brenguier et al*., 2000; *Grabowski*, 2006; *Jeffery*, 2007] and need to be considered when assessing the first indirect aerosol effect [*Pawlowska et al*., 2000].

Deep cumulus clouds are prevalent over the Indian summer monsoon region, and unraveling the raindrop formation mechanism is important for the monsoon cloud system. Thermodynamic and microphysical features of these clouds during the premonsoon (PRE) and monsoon (MON) conditions are discussed in *Prabha et al*. [2011, 2012a]. *Prabha et al*. [2011] report observations of the formation of precipitation size drops in MON clouds at lower levels above the cloud base compared to elevated levels in the PRE clouds. The study also documents larger cloud droplets present in less diluted region of these clouds, while entrainment-mixing in highly diluted cloud edge region decreases the liquid water content (LWC), mean radius, and droplet spectral width.

The objective of the present study is to document in more detail dynamical and microphysical properties of deep cumulus over the Indian subcontinent using in situ observations. The growing phase of a deep cumulus

is important for the understanding of warm rain process and cloud development. We contrast cumuli that develop in the premonsoon (PRE) conditions (i.e., highly polluted and dry environment) with those that develop in relatively clean and moist monsoon (MON) conditions. The manuscript first briefly reviews concepts involved in cumulus dynamics and entrainment-mixing processes. Subsequently, methods used to bring out salient features of the entrainment-mixing are discussed. Since the thermodynamic conditions corresponding to these cases are significantly different, we start our investigation characterizing the dynamical and thermodynamical influences on microphysical cloud parameters. Subsequently, we focus on the evolution of DSDs with respect to different types of mixing mechanisms (i.e., homogeneous versus extremely inhomogeneous) in the cloud core and at cloud edges. Investigations of entrainment and mixing are often criticized because of the relatively low spatial resolution of aircraft cloud observations, and present study argues that interpretation of the mixing characteristics may also depend on this aspect. We discuss entrainment effect on cloud microphysics as resolved by 1 Hz (about 100 m spatial scale) aircraft observation and source of entrained parcel in deep cumulus. We subsequently discuss higher-resolution aircraft observations (10 Hz; 10 m scale) and contrast them with the lower resolution results.

2. Methodology

This section provides a brief discussion of concepts and various analysis tools (variables, diagrams, etc.) applied in the discussion of data collected during the field project. They are introduced in the order they are applied in the subsequent sections.

Cumulative convective available potential energy (cCAPE) at a given height is defined as the integral of the positive buoyancy of a pseudoadiabatic parcel (i.e., assuming that all condensate falls out from the parcel) rising from near the surface throughout the atmosphere:

$$\mathrm{cCAPE}(z) = \int_0^z \max[0, B(z)]\mathrm{d}z \tag{1}$$

where the pseudoadiabatic buoyancy is $B(z) = g[(\theta-\theta_{\mathrm{env}})/\theta_{\mathrm{env}} + 0.61(q_v-q_{\mathrm{ve}})]$ with θ and θ_{env} (q_v and q_{ve}) is the potential temperature (water vapor mixing ratio) within the parcel and of the environment. CAPE is cCAPE (z_{LNB}) where z_{LNB} is the level of neutral buoyancy. We use cCAPE to highlight the difference in the pseudoadiabatic parcel properties near the cloud base for PRE and MON conditions.

For investigating the origin of the entrained parcels in observed cumulus clouds, we apply the *Paluch diagram* [*Paluch*, 1979]. The diagram applies two conserved thermodynamical variables, the total water mixing ratio Q, and the moist equivalent potential temperature θ_q which mix almost linearly during a mixing event. Present study uses the Paluch diagram with moist static energy temperature; T_h (the moist static energy divided by dry air heat capacity at constant pressure) instead of moist equivalent potential temperature [*Böing et al*., 2014]. The moist static energy and the moist static energy temperature remain conserved even when precipitation occurs as long as ice processes are absent. The moist static energy temperature T_h is derived as follows:

$$T_h = T + (gz + L_v q_v)/c_{\mathrm{pd}} \tag{2}$$

where T is the temperature, q_v is the water vapor mixing ratio, z is the height, L_v is the latent heat of evaporation and c_{pd} is the dry air heat capacity at constant pressure.

Paluch [1979] finds from aircraft observation that in-cloud points fall on a line that connects two points of the environment (cloud base and cloud top) and interprets that as the two-point mixing. Similar results are found by later studies [e.g., *Jensen et al*., 1985; *Reuter and Yau*, 1987], but some other studies show different source levels of the entrained air (i.e., lateral entrainment) using the same thermodynamic diagram [*Blyth et al*., 1988; *Raga et al*., 1990]. *Grabowski and Pawlowska* [1993] show that bias in aircraft measurements may lead to overestimation of the entrainment origin level.

The microphysical mixing diagram was introduced by *Burnet and Brenguier* [2007] to distinguish between various mixing scenarios in aircraft observations. In the diagram, droplet concentration N_d is plotted against mean volume diameter cubed r_v^3. The diagram is valid for the isobaric mixing between two parcels without activation of fresh CCN. The diagram becomes more ambiguous if the mixing is not isobaric or if in-cloud activation is present [*Krueger et al*., 2008]. Present study uses a modified diagram as in *Jarecka et al*. [2013]

to investigate entrainment and mixing with consideration of in-cloud activation that can be present as illustrated from the observations of *Prabha et al*. [2011, 2012a].

The extremely inhomogeneous mixing line on the mixing diagram is a simple horizontal line, that is, reduction of the droplet concentration without a change of the mean volume radius. The homogeneous mixing line is derived as follows. Droplet number concentration N_d is reduced according to the mass fraction χ of the entrained parcel, $N_d = \chi N_{d,a}$, and the mean volume droplet radius r_v decreases due to the saturation deficit and subsequent evaporation to bring the air back to saturation. The liquid water mixing ratio q_l, the temperature T, and the water vapor mixing ratio at saturation q_{vs} of the mixed parcel are calculated as [*Gerber et al*., 2008] follows:

$$q_l = \chi[q_{\mathrm{vsc}}(T_c) + q_{\mathrm{lc}}] + (1-\chi)q_{\mathrm{ve}} - q_{\mathrm{vs}}(T), \tag{3a}$$

$$T = \chi T_c + (1-\chi)T_e - \frac{L_c}{c_p}(\chi q_{\mathrm{lc}} - q_l), \tag{3b}$$

$$q_{\mathrm{vs}}(\mathrm{g/kg}) = \frac{3800}{p}\exp\left[\frac{L_c}{R_v}\left(\frac{1}{273} - \frac{1}{T}\right)\right], \tag{3c}$$

where L_c is the latent heat of condensation, c_p is the air heat capacity at constant pressure, the subscripts refer to properties of: *c*—the cloud, *e*—the environment, *l*—the liquid water, *v*—the water vapor, and *s* represents conditions at saturation. R_v is the gas constant for water vapor, T is the temperature (K), and p is pressure in hectopascal. By solving these equations for different values of χ, we can obtain the liquid water mixing ratio q_l for given values of the environmental relative humidity (RH) and temperature. The liquid water content (LWC) is derived by multiplying the liquid water mixing ratio q_l by the air density. Then the mean volume radius r_v is derived for a given droplet concentration from the relation $\mathrm{LWC} = \frac{4}{3}\pi\rho_w N {r_v}^3$, where ρ_w is the density of liquid water.

The characteristics of mixing depend on mixing time scale, τ_{mix} and evaporation time scale τ_{evap} [*Baker et al*., 1980; *Lehmann et al*., 2009; *Kumar et al*., 2012]. The evaporation time for a droplet of radius r is given by the following:

$$\tau_{\mathrm{evap}} = \frac{r^2[F_k + F_d]}{2S} \tag{4a}$$

where F_k and F_d are two thermodynamic constants [see *Rogers and Yau*, 1989, p. 102], and S is the water vapor saturation deficit. The time scale of turbulent mixing can be expressed as follows:

$$\tau_{\mathrm{mix}} \approx \frac{L}{U} = \left(\frac{L^2}{\varepsilon}\right)^{1/3}, \tag{4b}$$

where L is the linear extent (scale) of the mixed parcel, U is the turbulent velocity, and ε is the turbulent energy dissipation rate [*Baker et al*., 1984; *Broadwell and Breidenthal*, 1982].

The evaporation time scale τ_{evap} in equation (4a) may appear to be hypothetical in realistic clouds where an ensemble of cloud droplets evaporates together and influence the saturation field of other droplets. For this reason, another time scale has been introduced by the turbulent-mixing community and has been used instead of single droplet evaporation time τ_{evap}. The time scale is referred to as the phase relaxation time, τ_{phase} [*Lehmann et al*., 2009; *Kumar et al*., 2012a]. The time scale is the *e*-folding time at which a uniform volume with cloud droplets responds to an instantaneous supersaturation perturbation. Phase relaxation time scale τ_{phase} is given by the following:

$$\tau_{\mathrm{phase}} = \frac{1}{4\pi\delta N_d r}, \tag{4c}$$

where r is the mean radius of the population of droplets and δ is the diffusivity constant [e.g., *Kumar et al*., 2012]. Note, however, that τ_{phase} excludes the impact of the RH of the dry air involved in the mixing process. Thus, it is a matter of a debate which time scale is more appropriate for describing mixing characteristics in terms of the homogeneous versus inhomogeneous scenario.

The ratio of mixing time scales to phase relaxation time scale ($\tau_{\mathrm{mix}}/\tau_{\mathrm{phase}}$) is the cloud physics analog of the Damköhler number *Da* [e.g., *Dimotakis*, 2004; *Lehmann et al*., 2009; *Kumar et al*., 2012]. When the time scale of

turbulent mixing is much larger than the phase relaxation time ($\tau_{mix} \gg \tau_{phase}$, i.e., $Da \gg 1$), the turbulent stirring is slow and the boundary between cloudy air and subsaturated ambient air exists for a time sufficient for the total evaporation of droplets near the interface, while other droplets stay in saturated air and remain unchanged. This type of mixing is referred to as the extremely inhomogeneous mixing. In contrast, if turbulent mixing time scale is much smaller than the phase relaxation time scale ($\tau_{mix} \ll \tau_{phase}$ i.e., $Da \ll 1$), turbulent stirring is rapid; all droplets are exposed to the same subsaturation and partially evaporate simultaneously. In such a case, the droplet size distribution (DSD) shifts toward smaller sizes with either no change of the total droplet number or a reduction of the total number if the smallest droplets in the DSD evaporate completely. This is referred to as the homogeneous mixing.

To derive the mixing time scale in equation (4b), an estimate of the mixing length scale L is needed. For that, we analyzed aircraft observations at 10 Hz (i.e., approximately 10 m spatial scale). Two research flights observations from Cloud Aerosol Interaction and Precipitation Enhancement Experiment (CAIPEEX)-II on 3 November 2011 (RF45) and 6 November 2011 (RF47) are used because only 1 Hz data are available for other flights. The typical size of entrained eddies is assumed to be related to the size of diluted flight segments inside a cloud. Probability distribution function (PDF) analysis of the segments size is used to indicate possible mixing scale following *Krueger* [1993]. Observed liquid water content (LWC) from Forward Scattering Spectrometer Probe (FSSP) at 10 Hz is used. The size of a diluted segment is measured considering LWC along the flight path and assuming that segments with LWC above/below 50% of the highest observed LWC during a cloud pass are considered as an undiluted/diluted cloud segment, respectively. The PDF analysis is carried out for both cloud core and cloud edge regimes separately. A cloud core/edge of a cloudy volume is defined as in *Prabha et al*. [2012a] using the adiabatic fraction (AF), the ratio between observed LWC to its adiabatic value (LWC_{ad}) at 100 m spatial scale. The cloud core/edge is taken if AF is above/below 0.5.

3. The Field Experiment and Case Studies

Phase I and phase II of the Cloud Aerosol Interaction and Precipitation Enhancement Experiment (CAIPEEX) was conducted over India during May–September 2009 and September–November 2011, respectively, with several airborne instruments onboard a twin engine Piper Cheyene pressurized aircraft. The details of the phase I experiment are presented in *Kulkarni et al*. [2012]. The aircraft was equipped with a hotwire LWC probe (HWLWC-100; 0.0 to 5.0 g m^{-3} range), a Cloud Droplet Probe (CDP) for measurements of the cloud droplet size spectra in the range 2–50 μm, a cloud imaging probe (CIP) for the detection of precipitating particles and an Aircraft-Integrated Meteorological Measurement System (AIMMS)-20 probe for the measurement of temperature (in the range of −30°C to 50°C with a resolution of 0.01°C), humidity (range 5% to 100% with resolution of 0.1%), and vertical wind speed (with accuracy of 0.5 m s^{-1}). The temperature probe is designed to minimize the wetting effect inside the cloud by applying reverse flow. However, it still may be affected by wetting inside the cloud and may measure lower temperature as shown by *Lawson and Cooper* [1990] (this could not be ascertained). The phase II experiment was conducted mostly with the same instruments as 2009 except CDP is replaced by FSSP and operated at 1 Hz or 10 Hz (for few research flights). Radiosondes launched prior to the aircraft observations (at 06:00 UTC) are used to obtain vertical profiles of the wind, temperature, and water vapor mixing ratio which are used in the parcel model to calculate buoyancy and cCAPE.

Cloud profiling was performed on several constant level flights between the cloud base to cloud top, up to 7 km. Cloud condensation nuclei (CCN) were measured below the cloud base height at different supersaturation (SS) values (0.2, 0.4, and 0.6). Aircraft observations were mainly performed during local afternoon time (08:00 to 10:00 UTC) when convective clouds were developing due to strong solar insolation. Clouds were sampled mainly before the onset of precipitation in order to capture the impact of entrainment-mixing processes on precipitation formation. Some clouds grew much above the freezing level height at around 5 km. Mixed phase cloud regions above the freezing level were reported in *Prabha et al*. [2011].

Four case studies are examined in this paper, two from 2009 and two from 2011 experiment with one premonsoon (PRE) cloud (16 June 2009) and one monsoon (MON) cloud (22 June 2009) over Hyderabad (17.45°N, 78.46°E) and two other flights toward the end of monsoon (November 2011). These four cases have different thermodynamic and meteorological conditions. The boundary layer on 16 June was drier and warmer than in the 22 June case, but cloud layer environments were similar in terms of moisture and

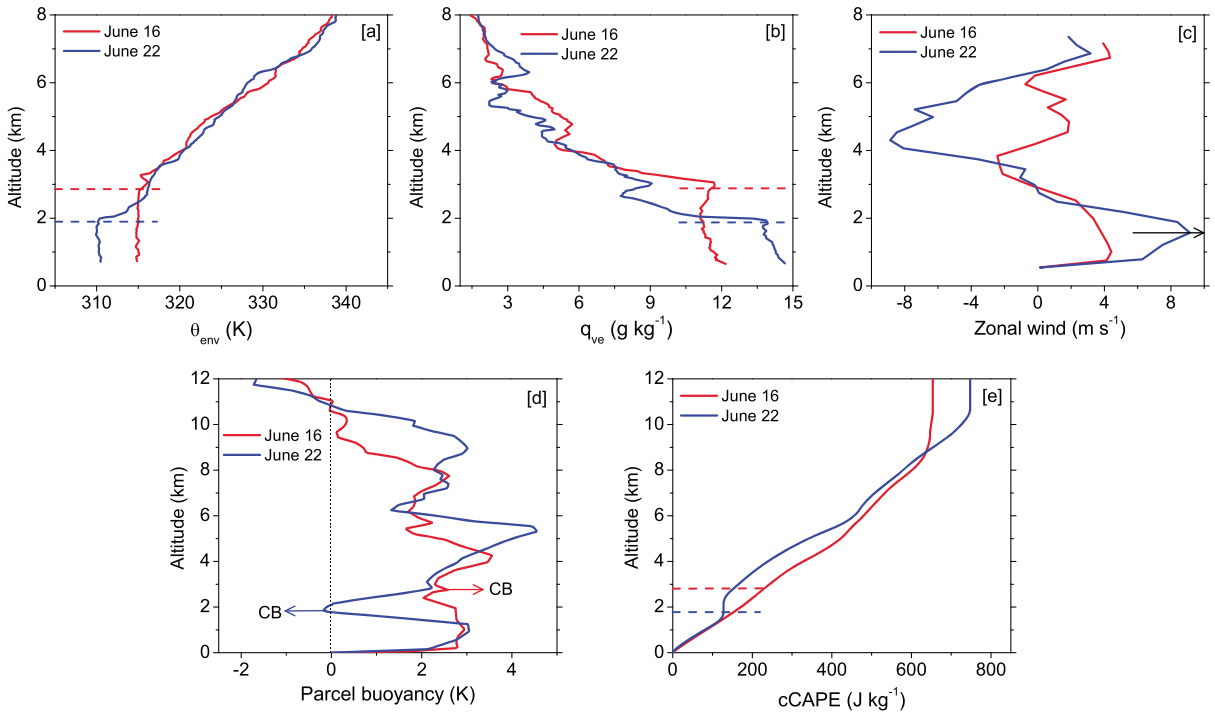

Figure 1. Vertical profiles of environmental (a) potential temperature (θ_{env}), (b) water vapor mixing ratio (q_{ve}), and (c) zonal wind (u) from radiosonde observation. (d) Vertical distribution of buoyancy of cloud parcel (in K), measured by the parcel model using the environmental sounding, [e] cumulative convective available potential energy (cCAPE) from the parcel model. The blue line represents 22 June case and the red line represents 16 June case. Jet core is indicated with an arrow in Figure 1c. Horizontal dashed lines in Figures 1a, 1b, 1e and arrows in 1d represent cloud base (CB) level for 16 June (red) and 22 June (blue), respectively. Vertical dashed line in Figure 1d corresponds to neutral buoyancy of the parcel.

temperature [*Prabha et al.*, 2011]. The subcloud CCN number concentration was higher for the PRE cloud (around 1070 cm^{-3} at 0.4% SS) compared to the MON cloud (around 340 cm^{-3} at 0.4% SS). Research flights used from CAIPEEX-II were conducted on 3 November (RF45) and 6 November (RF47) 2011 over Hyderabad and Mangalore (12.87°N, 74.88°E), respectively. These flights are deep convective cases, comparable to the MON cloud with cloud base at a low level (1.9 km and 1.3 km) and subcloud CCN concentration were around 860 cm^{-3} and 520 cm^{-3} (at 0.4% SS) respectively for RF45 and RF47.

4. Results

4.1. Thermodynamics and Microphysics

Transition from premonsoon (PRE) to monsoon (MON) conditions is unique because boundary layer thermodynamics change from day to day. Two flight observations (16 June for PRE and 22 June for MON, 2009) during this transition are analyzed here with special attention given to the differences in microphysical properties of convective clouds resulting from different thermodynamic conditions. These two case studies are representing the general characteristics of PRE and MON environment and have been used in many previous studies [e.g., *Prabha et al.*, 2011; *Bera et al.*, 2016]. The 16 June cloud was growing in a more polluted environment than the 22 June case. Thermodynamic and microphysical features are documented in Figures 1 and 2, respectively. Profiles of the environmental potential temperature (θ_{env}), water vapor mixing ratio (q_{ve}), and zonal wind (u) from radiosonde sounding taken prior to aircraft observation are presented in Figures 1a–1c. The figure shows that the well-mixed convective boundary layer is shallower in the humid MON case (less than 2 km) compared to the dry PRE case (the depth of 2.7 km). The monsoon low-level jet and associated moisture advection are both stronger for the MON case (Figure 1c). The MON case also has stronger vertical shear of the zonal wind between 1 and 5 km height. The vertical distribution of moisture is associated with the large-scale moisture transport by the monsoon low-level jet as well as the vertical mixing within the boundary layer. In the PRE case, the wind speed below 3 km is nearly half of the MON case, and the boundary layer is deep (about 2.7 km) and dry ($q_{ve} < 12$ g kg^{-1}). Thermodynamic conditions during other

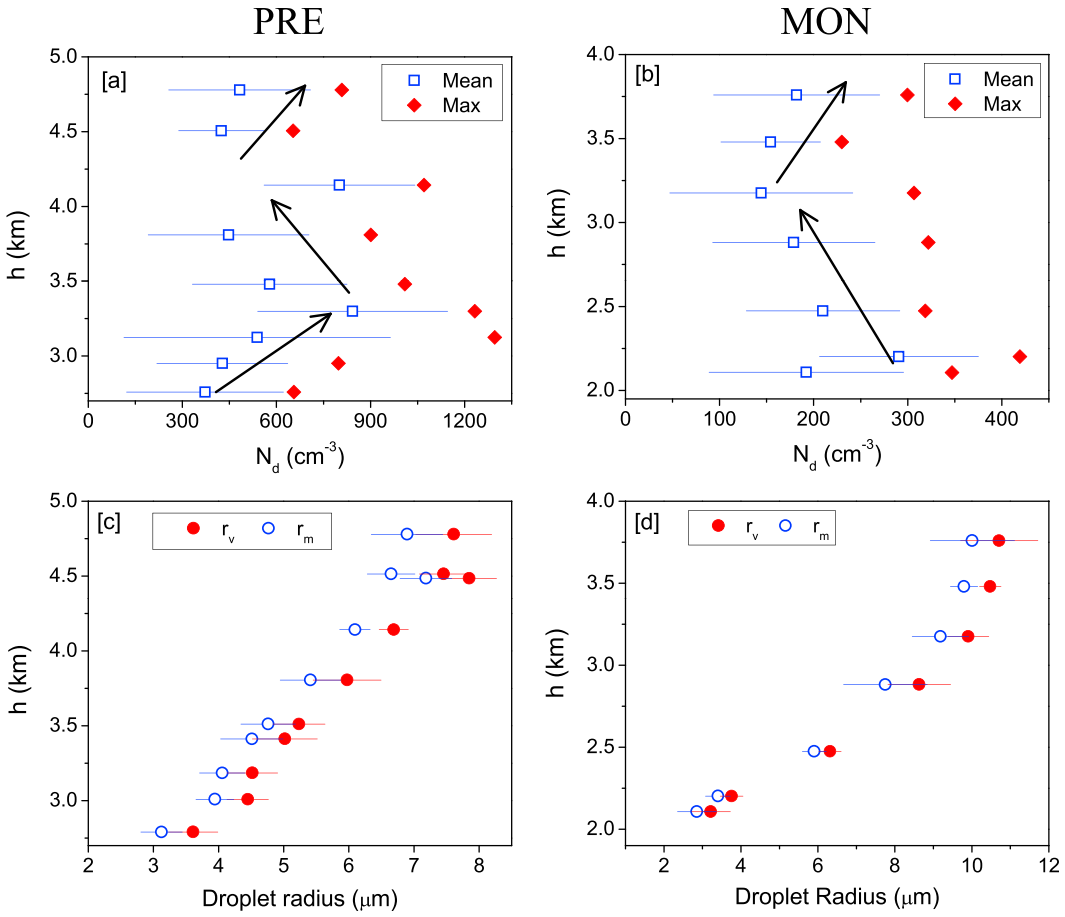

Figure 2. Vertical variation of mean and maximum cloud droplet number concentration (N_d), mean volume radius (r_v) and mean radius (r_m). Horizontal line (error bar) represents the standard deviation at each vertical level. (a and c) PRE case (16 June) is presented. (b and d) MON case (22 June) is presented.

two research flights analyzed in this study that correspond to the postmonsoon deep convection (research flights RF45 and RF47 in 2011) are presented in Figure S1 in the supporting information and are not discussed in detail. We only note that the boundary layer is even shallower for the postmonsoon cases with lower temperature and higher moisture at low levels. These are arguably resulting from reduced solar insolation and still relatively moist soil after the monsoon.

4.1.1. Parcel Model Analysis

Analysis of thermodynamic properties from a pseudoadiabatic parcel model for the two cases (16 and 22 June 2009) is presented in Figures 1d and 1e. In addition to the sounding data shown in Figures 1a and 1b, surface observations were used as an input to the parcel model. Parcel buoyancy is proportional to the difference of the density potential temperature between the parcel and the environment. Figure 1d shows distinct features for the PRE and MON clouds. For the PRE cloud, parcel buoyancy is approximately constant between the surface and 4 km above the ground (except close to the surface). In contrast, the buoyancy for the monsoon cloud shows a sharp decrease in the upper part of the boundary layer, reaching small negative values near the cloud base, and then it increases rapidly to reach values close to those for the PRE environment at 4 km.

Figure 1e shows vertical profiles of the cumulative convective available potential energy (cCAPE). Higher cCAPE is noted at cloud base level of the PRE case and linearly increases over several kilometers aloft. In contrast, cCAPE remains approximately constant for about 1 km above the cloud base for the MON cloud. The MON cloud regains more buoyancy above 3 km. However, the cCAPE is still lower than in the PRE case up to the height of about 9 km. The pseudoadiabatic CAPE (i.e., the asymptotic value of cCAPE) is relatively

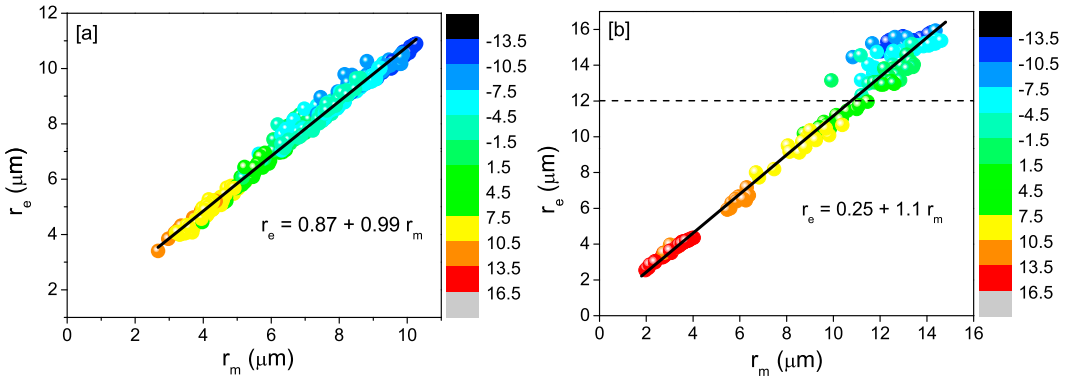

Figure 3. Correlation between effective radius (r_e) and mean radius (r_m) for entire flight on (a) 16 June and (b) 22 June. Temperature (°C) is indicated by color code. Dashed horizontal line in Figure 3b corresponds to 12 μm effective radius.

modest, around 700 J kg^{-1} for both cases, about 100 J kg^{-1} higher for the MON case. Parcel properties for postmonsoon cases are presented in the supporting information Figures S1c and S1d. Higher buoyancy and cCAPE is noted on 6 November 2011. Whether the thermodynamic features discussed above impact in-cloud microphysics, updraft motion and activation of CCN inside the cloud is discussed in the subsequent section.

4.1.2. Vertical Variation of Microphysical Parameters

Distribution of the droplet number concentration (N_d) and mean volume radius (r_v) statistics with height is depicted in Figure 2. Because there is less CCN available in the MON case, the droplet number concentration is lower and droplets are larger than in the PRE case. Indeed, the MON cloud formed drizzle size drops around 2 km above the cloud base height. Consequently, we restrict the analysis to drizzle-free levels as warm and nonprecipitating cloud regime is the focus. However, a few samples suspected to be contaminated by drops falling from above, as captured by the CIP images, have been rejected from the analysis. N_d (mean and maximum) in each 200 m vertical interval above cloud base is presented in Figures 2a and 2b for the PRE and MON cloud, respectively. The standard deviations at each height are represented by horizontal error bars; the maximum N_d encountered at each traverse is also shown. As one might expect, the PRE case shows higher N_d (the mean and the maximum) than MON at all levels because of the higher boundary layer CCN concentration. The PRE cloud produces maximum droplet number concentration at a height about 500 m above cloud base, while the MON cloud (Figure 2b) features the maximum just above the cloud base. Arguably, this can be explained by thermodynamic features of the two cases as discussed previously (cf. Figure 1). In the dry PRE case, cCAPE increases linearly above cloud base, and constant buoyancy can provide additional updraft strength leading to additional activation above the cloud base. In the MON case, however, the buoyancy is reduced near the cloud base, and cCAPE is almost constant for a few hundred meters above cloud base restricting the updraft strength. As a result, the increase in the droplet number concentration takes place in a shallow region near the cloud base where primary CCN activation occurs. Observations of the in-cloud updraft strengths above the cloud base, about 5 ms^{-1} in the PRE case and 2 ms^{-1} in the MON case, support this conjecture.

The arrows in Figures 2a and 2b show the increasing and decreasing tendency of the mean cloud droplet number concentration. Observations are only considered for warm and nonprecipitating cloud regions so the reduction of droplet number concentration due to collision-coalescence is insignificant. The droplet number concentration in the PRE case increases linearly up to a height of 0.6 km from cloud base and reaches values about twice larger than near the cloud base. Similar feature is observed in several other PRE cases not shown here. In contrast, the increase is smaller (about 50%) and limited to the cloud-base region of the MON cloud. Vertical distribution of the droplet number concentration for the two postmonsoon clouds is provided in the supporting information (Figure S2). The figure shows that the maximum droplet number concentration is at cloud base, and it decreases in the lowest kilometer above the cloud base.

Figures 2c and 2d present vertical profiles of the mean radius and the mean volume radius of cloud droplets. Larger droplets are seen in the MON cloud due to lower droplet concentration compared to the PRE cloud (see previous section). Droplet size increases approximately linearly with height in the PRE cloud, but the MON cloud shows a faster vertical variation at lower altitude and slower vertical variation at higher altitude

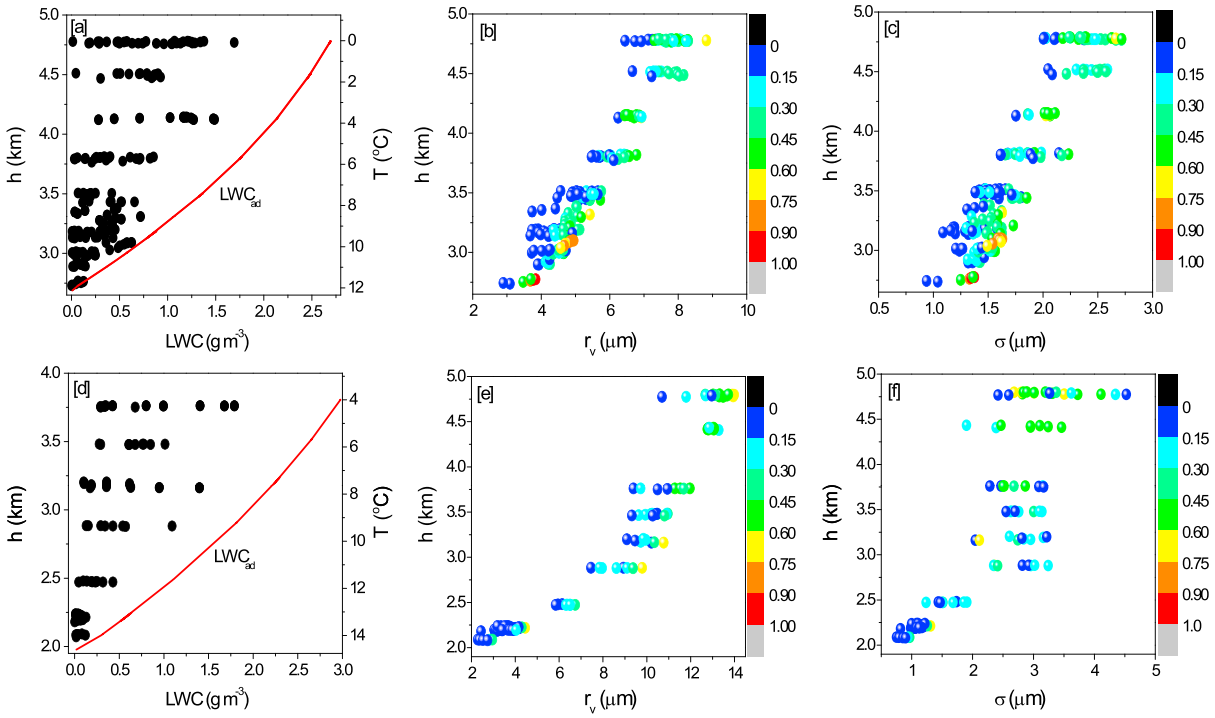

Figure 4. (a and d) Vertical fluctuation of 1 Hz LWC observation (black circle) above surface are shown. The solid red line represents adiabatic reference of liquid water content (LWC_{ad}). (b, e, c, and f) Vertical variation of mean volume radius (r_v) and droplet spectral width (σ) are presented. Figures 4a–4c and 4d–4f correspond to PRE case and MON case, respectively. The color code indicates adiabatic fraction (AF) of each sample at 1 Hz.

(e.g., approximately parabolic variation with height). This difference is likely due to the differences in the height dependence of the mean droplet number concentration, that is, the additional activation of droplets in the PRE case in the lowest few hundred meters above the cloud base. The variation of the mean radius at any specific level (indicated by the error bars) is higher for the PRE cloud, suggesting that droplet evaporation due to entrainment and secondary activation is more prevalent in these clouds, arguably in agreement with smaller droplet radius and high-CCN environment. The difference between the mean radius (r_m) and the mean volume radius (r_v) values (Figures 2c and 2d for the PRE and MON cases, respectively) remains almost constant with height in the PRE cloud, while it slightly increases in the MON case, suggesting broader droplet spectra at higher altitude levels [see *Prabha et al.*, 2011].

4.1.3. Microphysics of Rain Initiation

The correlation between mean radius (r_m) and effective radius (r_e) for the two cases is shown in Figures 3a and 3b to identify the level of raindrop formation [*Khain et al.*, 2013]. The intercepts of the linear fittings indicate that the difference between effective radius and mean radius is relatively smaller in the lower levels of the 22 June cloud but increases more rapidly (larger slope) with height compared to the 16 June cloud. The cloud on 22 June produces precipitation size droplets above 3.8 km altitude (i.e., about 1.8 km above cloud base). This is indicated in Figure 3b that shows a significant deviation of the effective radius from the mean radius after reaching 12 μm. The latter is considered a threshold for drizzle/rain initiation in ice-free clouds [*Pruppacher and Klett*, 1997; *Kulkarni et al.*, 2012; *Khain et al.*, 2013; *Bera et al.*, 2016]. Drizzle/rain drop formation at lower levels in a monsoon cloud makes the relationship between the r_m and r_e steeper due to production of larger (>12 μm) droplets and spectral broadening (the larger steepness is mainly due to larger droplet production above 4 km). Raindrops do not form in this PRE cloud, but there are indications for the ice phase to be active in this cloud near the cloud top. This aspect is not considered in the present study since the focus is restricted to warm regions of both clouds.

4.2. Entrainment Effects on Cloud Microphysics

The fluctuations of the LWC at various levels are shown in Figures 4a and 4d together with the adiabatic reference (solid red line). The deviation of LWC from adiabatic reference indicates that clouds are diluted due to

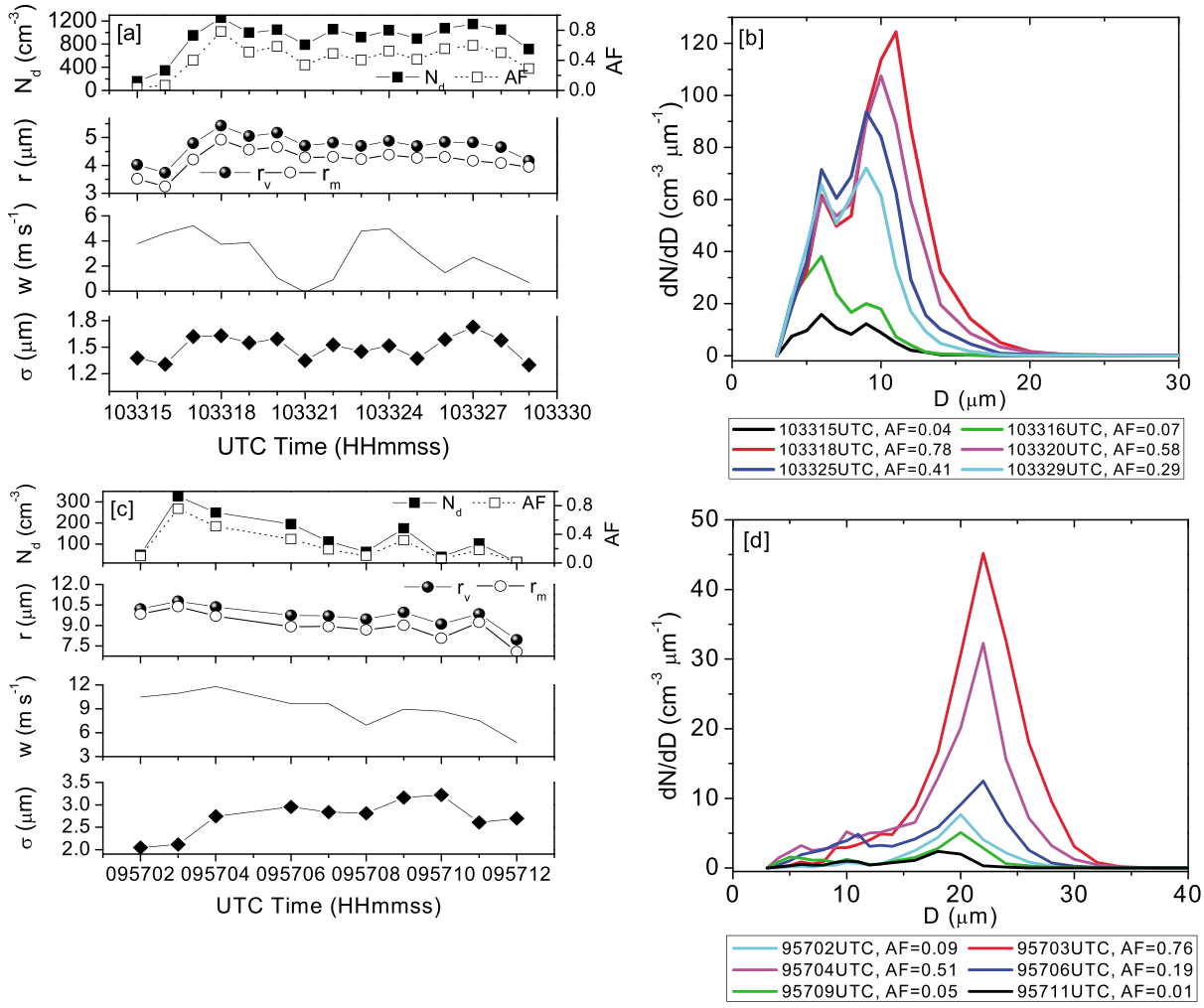

Figure 5. Variation of N_d, AF, droplet radius (r_v and r_m), vertical velocity (w), and spectral width (σ) along horizontal transects inside cloud (shown in the subpanels) at level (a) 3.1 km of 16 June and (c) 3.2 km of 22 June. (b and d) Droplet size distributions (DSDs) during the cloud passes on 16 and 22 June are presented. UTC time (hhmmss) of observation and corresponding AF of the samples are indicated in the legend below the DSD plots.

entrainment throughout the entire cloud depth, but especially so in upper levels. Variability of the mean radius and spectral width for selected cloud traverses across the PRE and MON clouds, stratified by the 1 Hz adiabatic fraction (LWC/LWC_{ad}), is presented in Figures 4b, 4c, 4e, and 4f. The adiabatic fraction is an indicator of the amount of entrainment. The mean radius is smaller/larger, in regions of lower/higher adiabatic fraction [e.g., *Prabha et al*., 2012a]. Spectral width seems to vary in the similar fashion for PRE cloud but not in the MON cloud where spectral width is relatively higher. The vertical variation of mean radius and spectral width have a nearly linear variation with height in the diluted regions and a parabolic variation with height (like in the averaged picture noted in the MON cloud, Figure 2d) in the regions of higher adiabatic fraction. This difference could be attributed to various aspects such as the environmental buoyancy, the droplet evaporation and activation, and to the aerosol number concentration. PRE case has a higher aerosol and CCN number concentration throughout the lower 5 km layer compared to the monsoon case [see *Prabha et al*., 2011, Figure 3]. The ratio between the spectral width, and the mean droplet radius, the relative dispersion, is higher in the PRE cloud when compared to the MON cloud [*Bera et al*., 2016].

Effects of entrainment on cloud microphysical properties at selected altitudes for the PRE and MON clouds are presented in Figures 5 and 6 using time series of microphysical parameters and corresponding droplet size distributions (DSDs). Figure 5 shows data from the PRE cloud on 16 June at 3.1 km (a and b) and for the MON cloud on 22 June at 3.2 km altitude (c and d). Data correspond roughly to 100 m spatial intervals. Figures 5a and 5c show the variation of the droplet number concentration (N_d), the adiabatic fraction (AF),

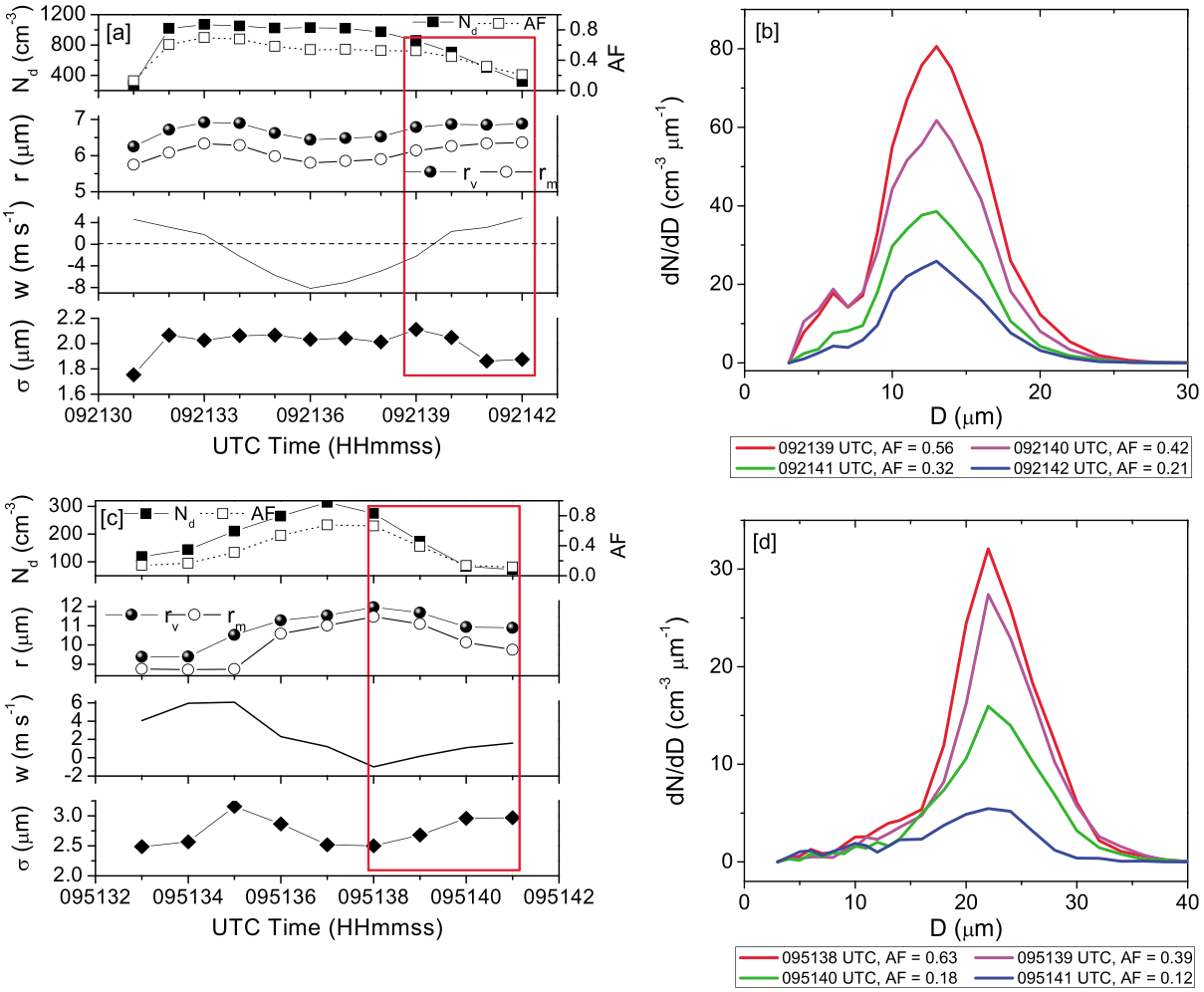

Figure 6. Same as Figure 5 but for two horizontal cloud transects at height level 4.1 km and 3.7 km of 16 June and 22 June, respectively. Here DSDs correspond to cloud edge samples in the region indicated by the red boxes.

the mean radius (r_m) and mean volume radius (r_v), vertical velocity (w), and the spectral width (σ; the standard deviation of DSD) along the flight track. DSD spectra corresponding to different in-cloud samples during the two cloud passes are displayed in Figures 5b and 5d. UTC time (in hour, minute, and second; hhmmss) and cloud liquid water dilution ratio (AF) corresponding to each droplet size distribution (DSD) are shown in the legend of Figures 5b and 5d.

During the two cloud passes (Figures 5a and 5c), clouds are seen strongly diluted at lateral edges with the cloud interior sustaining the highest LWC. In some instances droplet radius decreases at cloud edges, but in others it remains constant with higher values indicating different mixing stage. High values of the mean volume radii at cloud edges (Figure 5a, leading cloud edge at 103327 to 103329 UTC) may imply heterogeneous cloudy volume at the resolved scale (100 m), with dry air segments existing in-between cloudy segments at smaller scales than the one resolved. DSDs shift toward smaller sizes with reduced number concentration as dilution increases (cf. Figures 5b and 5d). This is more apparent in the PRE case (Figure 5 b). A relatively small shift for the MON case (Figure 5d) may indicate that mixing is at a transient stage, and the diluted cloudy volume has not been homogenized yet. The shift of DSDs toward smaller sizes with strongly reduced number density at cloud edge samples (lower AF) is a feature of intermediate mixing at its transient stage when smaller droplets have evaporated completely from DSD. The presence of inhomogeneous mixing at cloud edges (at scale of 100 m or larger) has been suggested by *Lehmann et al.* [2009] and *Freud et al.* [2011]. The least diluted droplet spectra for the PRE cloud (red colors in Figure 5b) are bimodal, with DSD peaks at around 7 and 11 μm.

Another aspect of aircraft observations at coarse resolutions is illustrated in Figure 6 (in the same format as Figure 5). Two cloud passes at 4.1 km altitude on 16 June and 3.8 km altitude on 22 June are shown (similar results are found at many other levels and the two shown here are representative). Microphysical parameter variations are shown in Figures 6a and 6c, whereas DSDs at different distances from the cloud core within red boxes in Figures 6a and 6c are presented in Figures 6b and 6d. In the two transects, the droplet mean volume radius remains almost constant at diluted cloud edge volumes despite increasing dilution and decreasing mean droplet concentrations. DSDs (Figures 6b and 6d) are similar to each other with a reduced droplet concentration at an increasing dilution. These may simply represent cases of the extremely inhomogeneous mixing as the spectra are similar with just a smaller total number. However, it is more likely that the aircraft went through heterogeneous volumes undergoing turbulent stirring (i.e., with subsegments of dry air in-between cloudy subsegments), and the increased dilution seen at 100 m scale merely represents increasing fraction of the cloud-free volume. Higher-resolution observations (at 10 Hz) are used later in this paper (section 4.4) to address this aspect.

4.3. Origin of Entrained Parcels

Entrained parcels were argued in the past to originate from either the cloud top [*Paluch*, 1979; *Reuter and Yau*, 1987] or from lateral cloud edges [*Blyth et al*., 1988; *Raga et al*., 1990; *Böing et al*., 2014]. Adapting the methodology proposed by *Paluch* [1979], we apply conserved thermodynamic variables, that is, the total water (liquid + vapor) mixing ratio (Q) and the moist static energy temperature (T_h) to find the origin level of dry air entrainment. Four observation levels (two from 16 June and two from 22 June) are examined in Figure 7 (other two research flights also showed similar results and are not presented here). Figure 7a is for the observation level at 3.2 km altitude of PRE (16 June) cloud. The figure shows that the mixing line (i.e., the least squares fit to the data points at 3.2 km) connects approximately the cloud base (CB) point and the point that has environmental properties close to or slightly below the observation level. Similar conclusion can be drawn from data at other flight levels shown in Figures 7b–7d. All mixing lines suggest that mixing has taken place between the cloud-base air and environmental air from the level not far from the observation level (same as *Blyth et al*. [1988]). However, there may be uncertainties due to unresolved variability of temperature and moisture with the 1 Hz data [see *Malinowski and Pawlowska*, 1989] or due to uncertainty of the temperature measurements [*Lawson and Cooper*, 1990]. Updrafts/downdrafts in Figure 7 are marked by the red/green arrows, respectively. The arrow size indicates the magnitude of updraft or downdraft velocity. The figure shows that mostly updrafts are seen for all levels except for observations at 4.15 km altitude where both updrafts and downdrafts are present. The mixing line on thermodynamic diagram indicates that lateral entrainment takes place from environmental levels that are close to the observation level in agreement with previous studies [*Blyth et al*., 1988; *Raga et al*., 1990; *Böing et al*., 2014].

The downdrafts observed for observational level at 4.15 km (Figure 7b) are not associated with penetrating downdrafts originating at the cloud top (about 7 km). They are found in volumes originating from the levels close to the observation level and are typically paired with updrafts, perhaps due to toroidal circulations typically observed in cumuli [e.g., *Damiani and Vali*, 2007] or circulations associated with interfacial instabilities [*Grabowski and Clark*, 1993a, 1993b]. These downdrafts could also be associated with in-cloud oscillations as suggested by *Prabha et al*. [2012b]. The mechanism of these oscillations is not understood. When air parcels descend due to oscillation, they experience subsaturation and start evaporating cloud droplets. The droplets mean radius decreases as seen in Figure 6a (092134 to 092139 UTC in cloud core). It is unlikely that these downdrafts originate from the cloud top (at 7 km height) because such downdrafts cannot penetrate significant downward distances inside the cloud as they quickly reach the level of neutral buoyancy [*Böing et al*., 2014]. Since the cloud tops in Figure 7 are a few kilometers above the observation levels [*Prabha et al*., 2011, 2012a], the thermodynamic diagrams do not indicate cloud top entrainment at much lower levels. Another possibility of not observing any penetrating downdraft from cloud top is due to the sampling of growing cumulus at its development stage.

The mixing line (least squares fit (LSF)) does not pass exactly through the cloud base point in Figure 7. This is due to the uncertainty in temperature measurement as the deviation of the mixing line from the cloud base temperature is within the uncertainty of temperature probe (1°C when LWC $\approx 2\,\mathrm{g\,m^{-3}}$) due to wetting [*Lawson and Cooper*, 1990]. Although the thermodynamic diagram suggests that clouds are mixed with its closest environment (two point mixing) through lateral entrainment, the conclusion is still uncertain.

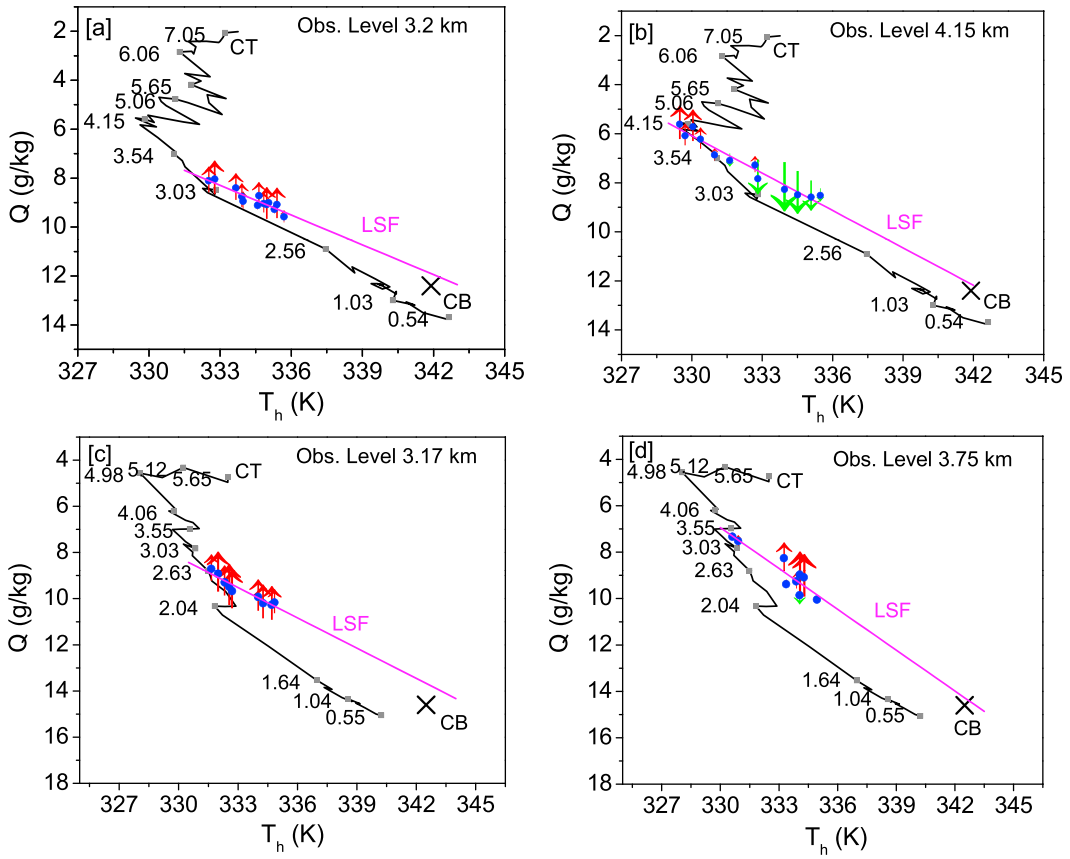

Figure 7. *Paluch* diagram for 16 June case with in-cloud observations at height levels (a) 3.2 km and (b) 4.15 km. Observation on 22 June at observation levels at (c) 3.17 km and (d) 3.75 km is also shown. Environmental sounding is represented by the black line and height levels (in km) are indicated by labels. The straight lines (least squares fit; LSF) represent the mixing line between two levels. In-cloud observation points are presented by blue markers (solid circle) on the diagram. Updraft and downdraft are represented by red and green arrows, respectively, and their magnitudes are presented by the size of the arrows. Cloud base (CB; with a cross) and cloud top (CT) levels are indicated on the diagram.

Böing et al. [2014] found from large eddy simulation study that the appearance of two point mixing (between the cloud base and close to observation level) on the thermodynamic mixing diagram can be misleading as particle trajectory obtained through the Lagrangian tracking documents mixing taking place at lateral edges from many levels.

4.4. Smaller-Scale Mixing and Microphysical Changes

In this section we discuss the impact of entrainment and mixing on cloud microphysics as observed at a finer scale applying 10 Hz observations in postmonsoon clouds. Two research flight observations are used, from 3 November (RF45) and 6 November (RF47) 2011. Vertical profiles of droplet mean volume radius (r_v) and spectral width (σ), stratified by AF values (at 10 Hz) are shown in Figure 8. There is a large increase of the data point number because of the higher sampling frequency. The more complicated vertical structure of observed clouds (especially in the RF45 case) likely comes from the fact that the aircraft sampled not a single cloud in both cases, but rather a cluster of clouds closely spaced together. The mixing analysis for RF45 presented later in this section comes from the upper region of the cluster, around 5 km, where only a single cumulus tower was encountered. In agreement with previous discussion (cf. Figure 4), 10 Hz data clearly show that the mean volumes radius increases with AF (a–c). Highly diluted samples ($AF < 0.15$) have the highest r_v spread (almost 50%) at each height level. There is a large variability and no obvious correlation between σ with AF as observed before for the monsoon cloud (Figure 4f).

4.4.1. Spatial Scales of In-Cloud Heterogeneities

It is clear that turbulent entrainment encompasses a wide range of spatial scales, from the scale of entraining eddies (hundreds of meters for a cumulus cloud) down to the molecular dissipation (the Kolmogorov scale),

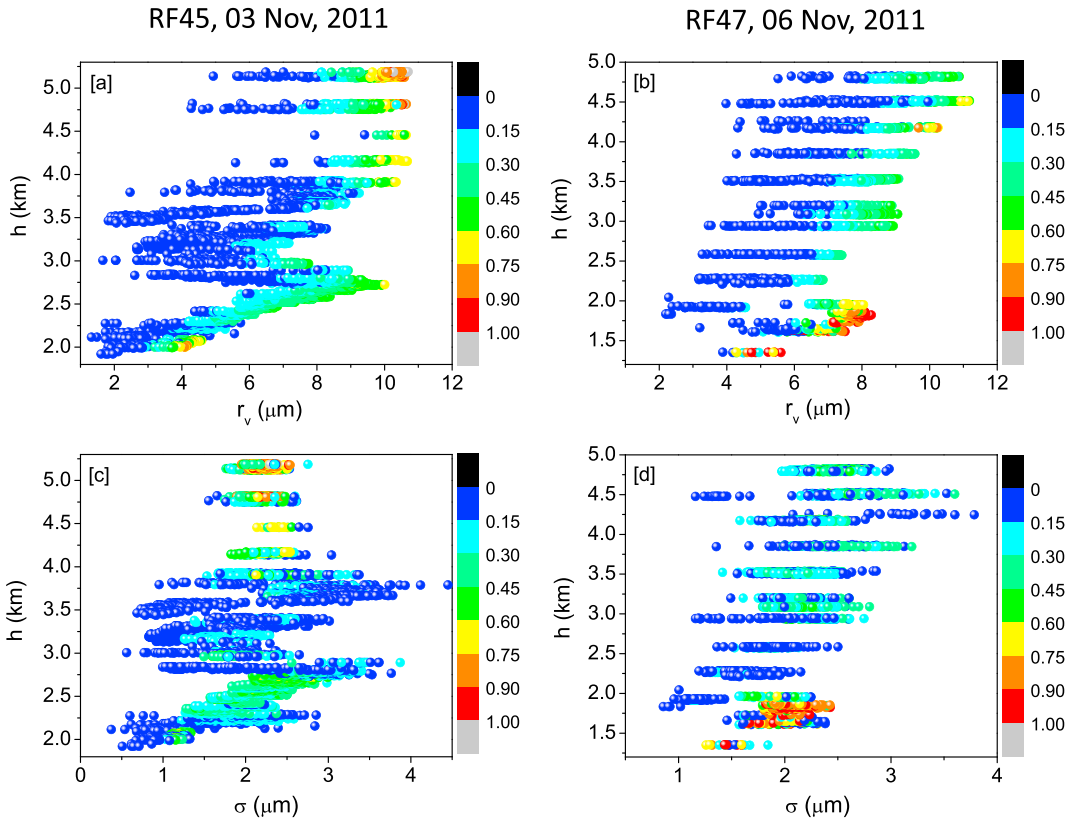

Figure 8. Fluctuations of mean volume radius (r_v) and DSD spectral width (σ) in vertical plane as seen from 10 Hz observation for clouds during research flight (a and c) RF45 and (b and d) RF47. Color bars indicate AF values.

around 1 mm in typical cloud conditions. Typical aircraft observations (say, in the range of 1 to 10 Hz) can only resolve upper end of this range, and it is difficult to expect that homogeneous volumes are sampled by the aircraft instrumentation. Only some special instruments (like the Fast FSSP or Particulate Volume Monitor (PVM) for the cloud water or Ultra-Fast Thermometer (UFT) for the temperature [e.g., *Gerber et al.*, 2005]) can approach small-scale end of the range. Nevertheless, aircraft observations at 10 Hz can be used to estimate large-end scales characterizing cumulus entrainment, an aspect discussed in this section.

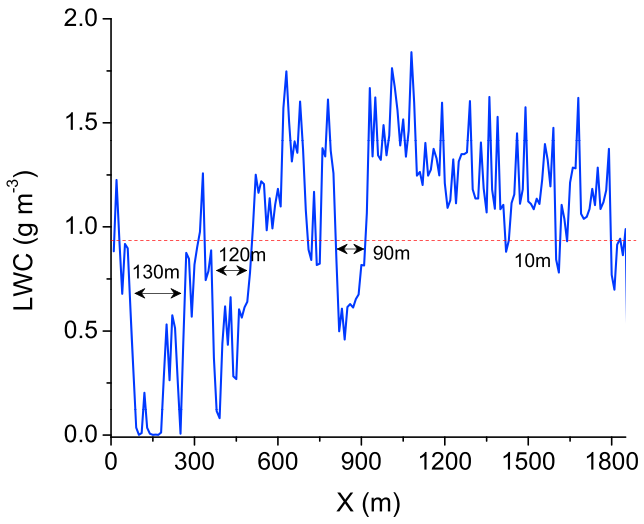

Figure 9. Fluctuations of cloud liquid water content (LWC) during a cloud transect (horizontal pass) at 3.1 km altitude of RF47. The identification of unsaturated parcel size is indicated with LWC below threshold of 50% of maximum LWC (indicated with dashed line) during the cloud pass.

An example of LWC fluctuations at approximately 10 m resolved scale (10 Hz) by the Forward Scattering Spectrometer Probe (FSSP) during a cloud pass at 3.1 km altitude (without the precipitation size drops) is presented in Figure 9. The figure illustrates different scales for LWC variability along the flight path. Near the cloud edge (left part of the figure) large-amplitude fluctuations, from close to zero to not far from the maximum LWC encountered inside the cloud at larger-scale, are present. While smaller-scale fluctuations, with amplitudes around 10% of the maximum LWC, are evident in the

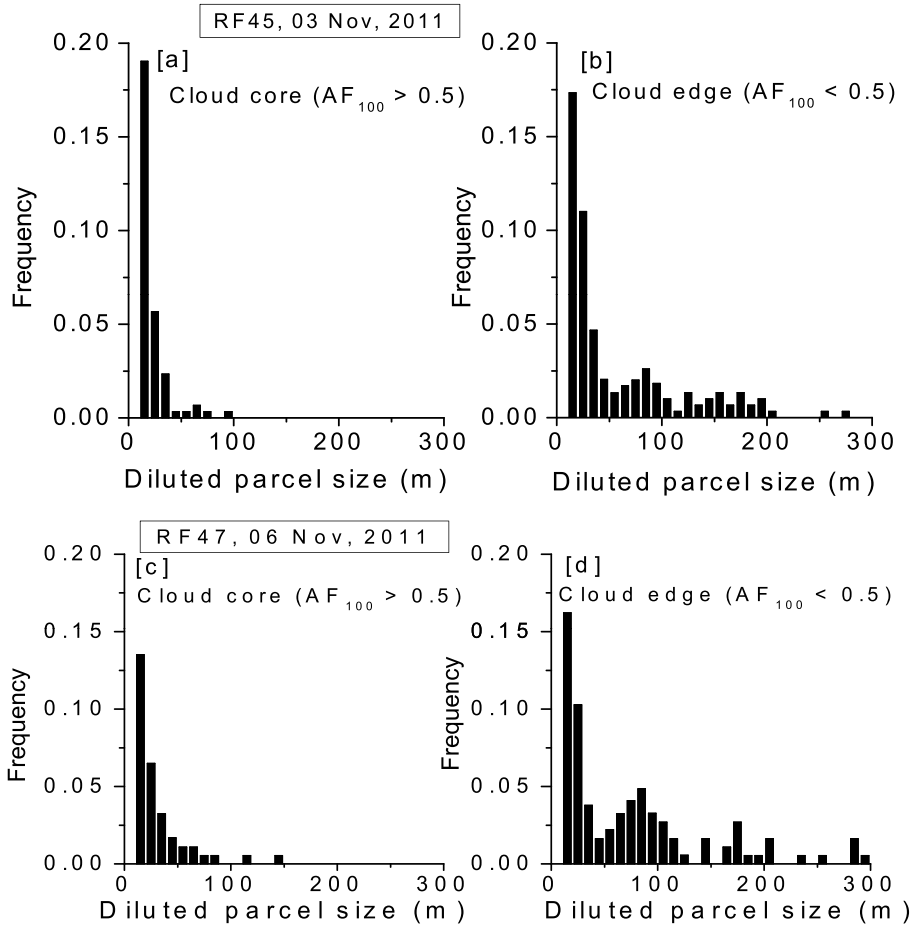

Figure 10. Probability distribution function (PDF) of diluted parcel sizes for cloudy volume with (a and c) AF $>$ 0.5 in 100 m segments and for cloudy volume with (b and d) AF $<$ 0.5 in 100 m segments during two research flights, RF45 (Figures 10a and 10b) and RF47 (Figures 10c and 10d).

middle of the figure (cloud core). The figure shows that the cloud edge mixing happens at scales of the order of 100 m, and LWC fluctuations are at much smaller scale (10–20 m) inside the cloud core. Probability distribution function (PDF) of scales (with range of 10 m to few hundred meters) of diluted segments is presented in Figure 10 for the two entire flights RF45 and RF47 applying 10 Hz observations. Here the diluted segment is defined as a cloud volume (10 m segment) with LWC less than 50% of the highest observed LWC (LWC_{max}) during the cloud pass [*Krueger et al.*, 2008]. The red dashed line in Figure 9 corresponds to 50% LWC_{max} line. In Figure 10, PDFs of the diluted parcel size are derived separately for the cloud core and cloud edge regimes. Cloud core and cloud edge are defined, respectively, as cloud samples with AF $>$ 0.5 or AF $<$ 0.5 at the 100 m spatial scale similar to *Prabha et al.* [2012a]. It should be noted that AF larger than 0.5 at the 100 m spatial scale can still have smaller-scale fluctuations reaching AF values below 0.5 as illustrated by couple instances in the right side of Figure 9. The PDFs in Figure 10 show that the size of a diluted segment peaks at small (10–20 m) scales for the cloud core regime. The PDFs have a broad range (10 m to few hundred meters) for the cloud edge regime. There is a second peak at scales close 100 m or slightly less for the cloud edge regime. This indicates that mixing is dominated by LWC fluctuations around 100 m scale (arguably the typical entrainment scale) for cloud edge. Subsequent turbulent stirring leads to the formation of smaller-scale fluctuations (down to the microscale), with only a small fraction is detectable by still relatively low-resolution 10 Hz observations. Both flights show similar PDF features and indicate valuable information of mixing scale in cloud edge and cloud core.

4.4.2. Changes in Microphysical Parameters

Keeping the mixing scale distribution in mind, we now discuss microphysical changes due to small-scale mixing, modification of droplet size spectra (DSD), and characterizing the mixing types (homogeneous versus

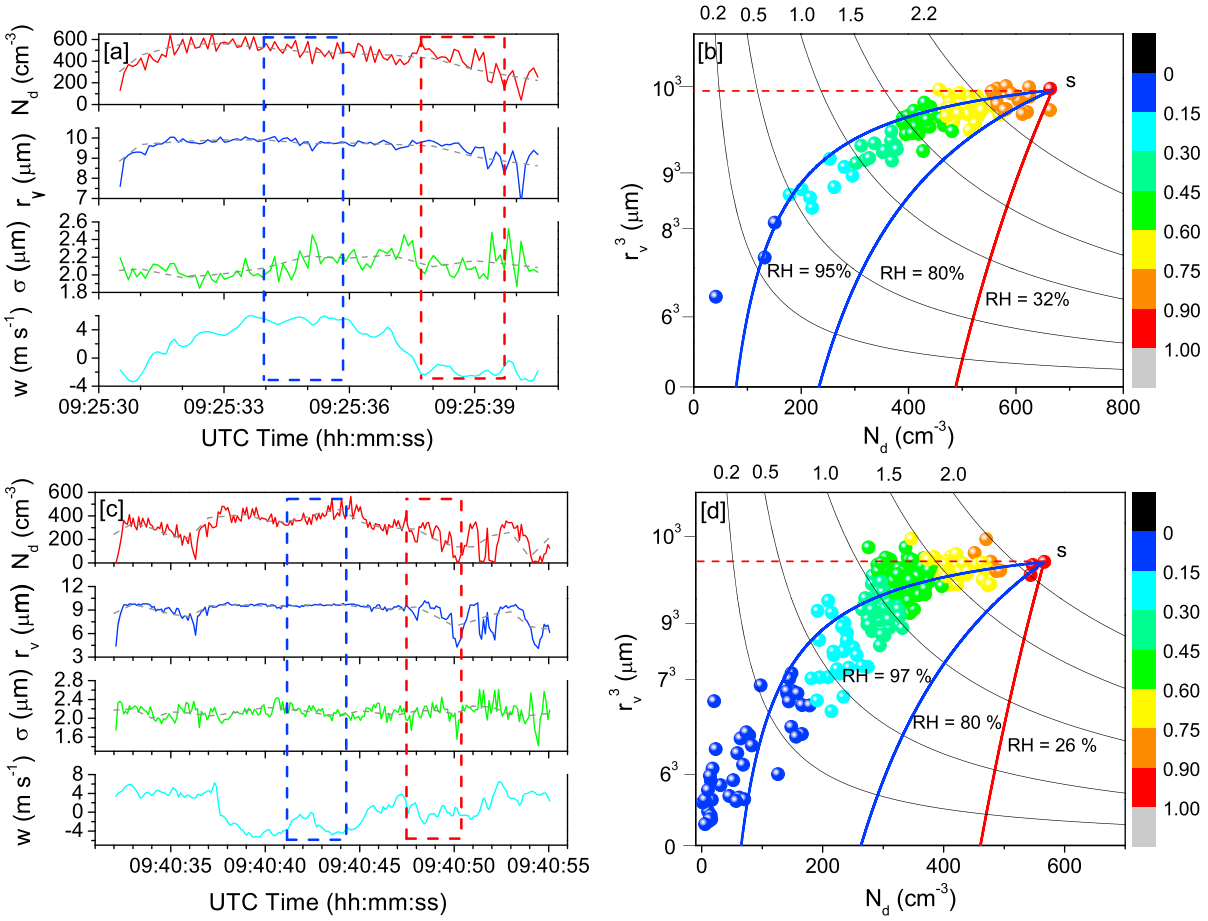

Figure 11. Distribution of microphysical parameters (N_d, r_v, and σ) and vertical velocity (w) during two horizontal cloud transects at 10 Hz resolution (≈10 m segment) at altitude of (a) 5.1 km and (c) 4.8 km during RF45. Dashed gray lines show mean distribution at 100 m scale. (b and d) Microphysical mixing diagrams for the same height levels. Color indicates different values of AF at 10 Hz. Hyperbolic black lines correspond to constant LWC line (0.2 to 2.2 gm^{-3}), red dashed line indicates the extremely inhomogeneous mixing line, and red and blue solid lines indicate the homogeneous mixing line for the environmental RH and higher RHs, respectively.

extremely inhomogeneous). The 10 Hz in situ observations are used to study features at 100 m spatial scale. Distribution of N_d, r_v, σ, and w inside the cloud during horizontal cloud passes are displayed in Figure 11. Two cloud passes at altitude of 5.1 km and 4.8 km from RF45 are shown in Figures 11a and 11c, respectively (note that as shown in Figure S2, these two levels have the maximum LWC close to adiabatic, so the uncertainty in the mixing diagram is minimized). The 100 m scale averaged values (gray dashed lines) of each parameter are also shown with the 10 Hz observations. As the figures show, there are small-scale fluctuations of each parameter, but the 100 m averaged values vary smoothly.

At cloud edges (right side of Figures 11a and 11c), N_d and r_v fluctuate significantly at 10 Hz, but their gradual decrease toward cloud edge is evident at 1 Hz (100 m) data. This is a drawback of 1 Hz observations as discussed before (section 4.2). The cloud edge is typically dominated by cloud downdrafts. In the cloud core with the strongest updraft, N_d fluctuates at small scales, whereas r_v is nearly constant. Because the cloud core is almost undiluted, the N_d fluctuations may come from observational uncertainties (e.g., statistical fluctuations of FSSP measurements), nonnegligible entrainment, differences in the droplet activation at the cloud base or above it (e.g., due to variations of the vertical velocity) or from a combination of all of them. The spectral width σ fluctuates both at the core and at the edges, but the fluctuations are larger near the edges as one might expect.

Figures 11b and 11d present data from the passes using microphysical mixing diagram as used by *Burnet and Brenguier* [2007] and modified by *Jarecka et al.* [2013]. In-cloud 10 Hz samples are stratified on the mixing diagram by AF (color scale) to distinguish strongly and weakly diluted samples. Theoretical homogeneous mixing line assuming the environmental temperature and RH at the flight altitude is represented by the solid red

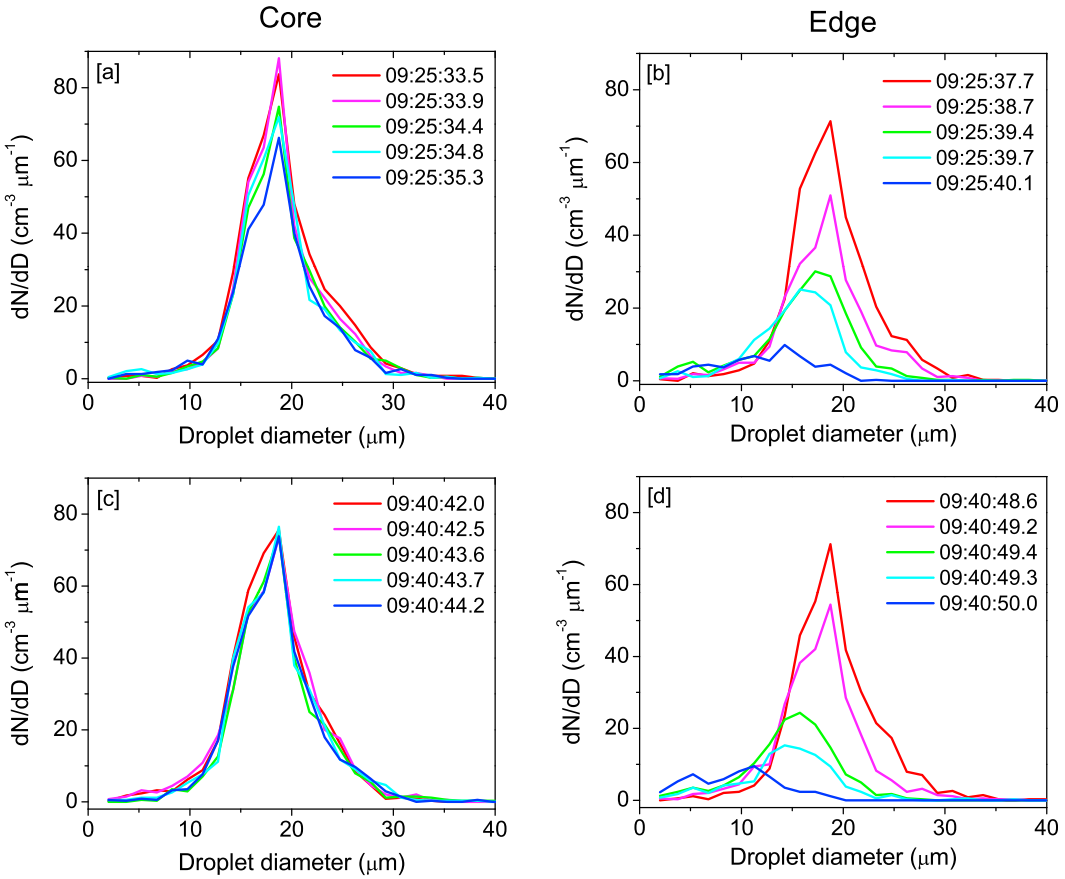

Figure 12. DSDs at different instances of cloud passes in (a and c) cloud core region and (b and d) cloud edge region for two height levels, 5.1 km (Figures 12a and 12b) and 4.8 km (Figures 12c and 12d) for RF45. UTC time (hh:mm:ss) of observation is indicated in figure legends.

line. In addition, several homogeneous mixing lines are also shown for higher RH values using solid blue lines. Cumulus clouds are often observed to feature a shell of descending air with enhanced RH [e.g., *Heus et al.*, 2009], and it is possible that air from the shell is involved in the entrainment, not the air from the far environment. The extremely inhomogeneous mixing is represented by horizontal dashed red line. Constant LWC lines are black hyperbolas. Mixing on the diagram starts from the point corresponding to the highest droplet concentration (N_d) and LWC (the latter is close to the adiabatic value for both the passes). The mixing diagram shows, in-cloud samples are mostly falling between the homogeneous line for the environmental RH and the extremely inhomogeneous line. The points seem to be also aligned along the homogeneous mixing line for high RH, so one can interpret the diagram as suggesting homogeneous mixing with the air from the descending shell. Moreover, one needs to keep in mind that observed samples are likely not homogenized down to the microscale, but they still undergo turbulent stirring.

DSDs within cloud core and cloud edge as indicated by blue and red box in Figures 11a and 11c are shown in Figure 12. Figures 12a–12b and 12c–12d correspond to clouds sampled during RF45 at altitude of 5.1 km and 4.8 km, respectively. Figures 12a and 12c are for the cloud core, and Figures 12b and 12d are for the cloud edge. The main feature for the cloud core is that DSDs are almost the same, except for small variations in the concentration. For cloud edge, DSDs shift toward smaller sizes with reduced droplet concentrations as dilution increases. The shift implies some evaporation, whereas reduced droplet concentration may come from either evaporation of the DSD's small droplets or from still unresolved structures (i.e., cloud-free filaments present within the coarsely mixed volumes), or both.

Additional cloud passes from research flight on 6 November 2011 (RF47) at altitude of 2.1 km and 4.5 km are shown in Figure 13. The results are similar to those shown in Figure 11 (RF45). Evolutions of microphysical

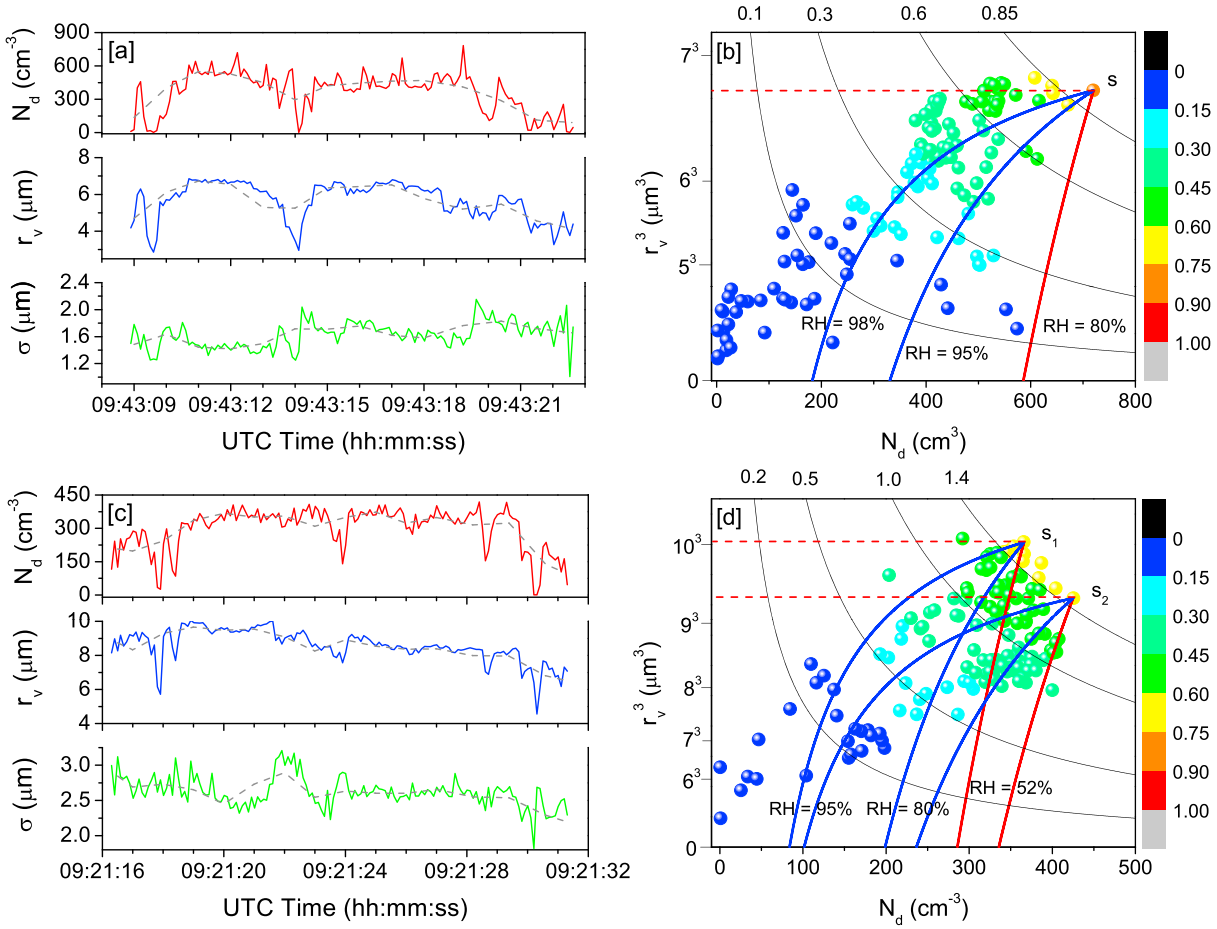

Figure 13. Same as Figure 11 (except for vertical velocity) for two height levels, (a and b) 2.2 km and (c and d) 4.5 km during RF47.

parameters (N_d, r_v, and σ) during the cloud passes are shown in Figures 13a and 13c. Vertical wind for this flight is not available. Microphysical mixing diagrams similar to Figures 11b and 11d are also presented. Environmental RH during this flight was relatively high, at 80% and 52% at 2.1 and 4.5 km, respectively. Mixing diagrams for the two levels during RF47 are similar to those from RF45 (Figure 11), except for a larger scatter of data points and thus lack of clear alignment along high RH homogeneous mixing line. For the cloud pass at 4.5 km (Figures 13c and 13d), N_d varies for the highest LWC and choosing the starting point is difficult as none of the volumes are close to adiabatic. Instead of choosing a single start point, we select two start points that span the range from the highest N_d to the highest r_v on the highest LWC line [see *Jarecka et al.*, 2013]. The data points seem to align along two distinct mixing lines that fit the high RH homogeneous mixing line poorly when compared to Figure 11. DSDs spectra for the cloud passes shown in Figure 13 are similar to those shown in Figure 12 and thus are not shown.

4.4.3. Estimation of Relevant Time Scales

PDF analysis of the diluted parcel size (Figure 10) strongly suggests that cloud edge mixing starts at a length scale of around 100 m. This estimate agrees with results of *Raga et al.* [1990] who found the typical entrainment length scale of a few hundred meters in cumulus cloud near Hawaii. *Krueger et al.* [1997] and *Su et al.* [1998] suggested length scales of 50 to 200 m as an approximate size of entrained blobs. The length scale in the cloud core is much smaller, 10–20 m, although the mixing in the core is insignificant as there are virtually no changes of the DSD spectra. We estimate the mixing time scale for the cloud edge region assuming the length scale of 100 m. The mixing time scale is estimated as $\tau_{mix} \approx L/U$ (equation (4b)), where U is the root-mean-square (RMS) vertical velocity $U = \sqrt{\overline{w.w}}$, where the vertical velocity w is measured at 10 Hz by the AIMMS probe. The RMS vertical velocity at the cloud edge is derived at approximately 2.6 m s^{-1} (see Figure 11). Using these values, τ_{mix} is

found to be about 38.5 s. The corresponding turbulent kinetic energy dissipation rate ε is about $17.5 \times 10^{-2}\,m^2\,s^{-3}$.

As discussed in section 2, there are two time scales that together with τ_{mix} can be used to estimate the Damköhler number: the droplet evaporation time scale τ_{evap} and the phase relaxation time scale τ_{phase}. For the evaporation time scale τ_{evap}, we assume mixing starts at the adiabatic droplet radius, and the droplet evaporates as the cloudy air mixes with dry air from the environment. The saturation ratio of dry air is same as that of the environment when mixing starts. Evaporation time scale using equation (4a) is an appropriate estimate for a single droplet in an unsaturated air, but actual situation in real clouds is different as many droplets evaporate at same time and they influences the saturation ratio. Thus, the phase relaxation time scale as estimated using equation (4c) might be more appropriate. However, applying appropriate numerical values for the environmental humidity (indicated on Figure 11), droplet radius (around 10 μm), and number concentration (around 550 cm^{-3}) results in τ_{phase} and τ_{evap} relatively close to each other, between 1 and 2 s. These estimates imply that mixing time (τ_{mix}) scale is much higher than either the evaporation time scale (τ_{evap}) or the phase relaxation time scale (τ_{phase}) and mixing is likely to be not far from the extremely inhomogeneous, in contrast to what Figures 11 and 13 suggest.

5. Discussions and Conclusions

This study investigates the microphysics of deep cumulus clouds observed over the Indian monsoon region and their links to the boundary layer thermodynamics for two case studies representative of the dry, high aerosol premonsoon (PRE) case and the moist, low aerosol monsoon (MON) case. Parcel analysis suggests that cloud buoyancy is relatively uniform across the boundary layer and lower part of the convection layer in the PRE case. This arguably leads to a continuous acceleration of a cloudy volume across the cloud base and just above it (i.e., cumulative CAPE increases linearly above the cloud base). We suggest that this feature leads to an additional activation of CCN above the cloud base and results in the increase of the observed mean and maximum cloud droplet concentration in the few hundred meters above the cloud base. In contrast, the MON case features parcel buoyancy decreasing to almost zero near the cloud base and then increasing rapidly within several hundred meters above the cloud base (i.e., cumulative CAPE almost constant within a kilometer above the cloud base). As a result, the mean and maximum droplet concentrations tend to decrease above the cloud base.

The mean radius features approximately linear increase with height in the PRE cloud compared to a faster (parabolic) vertical increase in the MON cloud. The vertical evolution of droplet number concentration in MON can also be influenced by the collision-coalescence that becomes active at a lower elevation (around 2 km above the cloud base) in monsoon clouds [*Konwar et al*., 2012]. Ice process, not considered in the current study, plays a significant role in the PRE case.

Application of the thermodynamic [*Paluch*, 1979] diagram to identify possible entrainment origin levels in monsoon convective clouds suggests that entrainment originates from levels within a few hundred meters from the observation level (Figure 7). However, these measurements may suffer from measurement uncertainty, for instance, due to wetting of the temperature probe. Although the analysis of the thermodynamic diagram indicates lateral entrainment from a level close to the observation level, this can be a wrong interpretation as *Böing et al*. [2014] showed from Lagrangian particle tracking. The lack of cloud top entrainment as deduced from the thermodynamic diagram can result from sampling actively growing cumuli in the developing stage where lateral entrainment dominates. The picture may be different if clouds are sampled at the dissipation stage.

In agreement with numerous previous studies (some discussed in section 1), cloud microphysical properties are significantly influenced by entrainment-mixing processes. Liquid water and droplet number concentration decrease in the cloud edge region that is strongly affected by entrainment (at scales of 100–300 m in the case of relatively narrow convective clouds investigated here). Inside clouds, away from cloud edge, the fluctuations are smaller and at smaller scales. The latter may reflect either effect of smaller dilution or turbulent stirring closer to the homogenization, or both. Smaller droplets are observed in diluted cloud volumes (i.e., at lower adiabatic fractions) where entrainment leads predominantly to droplet evaporation. This is especially clear with the 10 Hz data (cf. Figure 8). Spectral width of DSD as observed at 1 Hz (i.e., around 100 m scale, Figure 4) may suggest lower values in the highest diluted cloud samples, but 10 Hz data clearly show

the lack of a clear relationship between spectral width and AF. This perhaps should not be surprising considering the multiscale nature of turbulent mixing processes and still relatively low spatial resolution of the aircraft observations.

DSDs examined for diluted cloud edge and undiluted cloud core regions differ significantly. For the cloud edge, DSDs are shifted toward smaller sizes with reduced droplet number concentration as dilution increases (Figures 12b and 12d). The shift is associated with complete evaporation of small droplets and partial evaporation of larger droplets. Since smaller droplets evaporate faster compared to larger droplets, the DSD shape changes significantly (i.e., the width increases). For cloud core volumes, on the other hand, DSDs are almost identical with slight fluctuation in the droplet number concentration (Figures 12a and 12c). The largest droplets are formed in cloud cores as indicated by *Khain et al*. [2013], and production of superadiabatic droplets is not favored by the inhomogeneous mixing at diluted cloud edges as hypothesized in some studies [e.g., *Paluch and Knight*, 1984; *Paluch and Baumgardner*, 1989; *Korolev and Isaac*, 2000].

Analysis of diluted parcel length scales suggests that the mixing scale at the cloud core is around 10–20 m, but at lateral edges the scale is significantly larger, 100–200 m. With those length scales, the turbulent mixing time scales are 1 to 2 orders of magnitude larger than the droplet evaporation time scale (the latter is close to the phase relaxation time scale). This implies that the mixing should be close to the extremely inhomogeneous [e.g., *Lehmann et al*., 2009; *Andrejczuk et al*., 2009]. However, mixing diagrams shown in Figures 11 and 13 suggest intermediate mixing or possibly mixing close to homogeneous with high RH air that comes from the descending shell at the cloud edge. This situation is similar to the one discussed in *Yum et al*. [2015] using the aircraft measurements of marine boundary layer stratocumulus clouds over the southeastern Pacific. They show that the time scales of mixing and of droplet evaporation imply the inhomogeneous mixing, arguably consistent with stratocumulus' low turbulence intensity, yet the observations typically suggest homogeneous mixing. *Yum et al*. [2015] suggest a possible physical mechanism leading to such a discrepancy. We are not ready to speculate on the origin of the differences seen in our analysis beyond simply to suggest that perhaps the ideas based on the mixing of two air parcels have limited applicability to turbulent mixing between a deep cumulus cloud and its environment.

Observations discussed in this paper prompt us to suggest that mixing in the deep cumulus could be considered as a two-step process, where the lateral entrainment, with features akin to the inhomogeneous mixing due to unresolved smaller-scale structures, takes place at cloud edges, and the cloud core, only weakly influenced by the lateral entrainment and thus maintaining positive buoyancy, emerges as much closer to being homogenized. The raindrop formation is unlikely to be affected by the first step of the mixing process or higher-resolution data may be required to prove that aspect. In particular, superadiabatic droplets cannot form because reduced droplet concentrations (the corner stone of the superadiabatic growth hypothesis) are just artifacts of insufficient spatial resolution of the measurements. Adiabatic drops are present in weakly diluted convective cores, and they are sufficient to explain drizzle/rain formation in the monsoon clouds (Figure 3), whereas both warm-rain and ice processes lead to precipitation formation in the premonsoon (and likely postmonsoon, not shown) deep cumulus clouds [*Khain et al*., 2013].

Droplet size spectra suggest that the formation of the larger droplets mainly occurs in the cloud cores that are less influenced by entrainment-mixing. Similar conclusion was reached through analysis documented in *Prabha et al*. [2012a] and in numerical simulations of *Khain et al*. [2013]. The detailed analysis presented in this study shows that lateral entrainment and turbulent mixing plays a minor role for the onset of precipitation in monsoon deep convective clouds. However, small-scale mixing may still play some role in the cloud core contributing to the variance of the droplet number concentrations and spectral shape.

One of possible suggestions for the future research stemming from observations and analyses discussed herein is to look closer at the properties of the descending shell and attempt to untangle the mixing characteristics dilemma as discussed above. We hope to report on such a study in future publications.

Acknowledgments

CAIPEEX project and IITM are fully funded by Ministry of Earth Sciences (MoES), Government of India, New Delhi. CAIPEEX data are property of MoES, India, and are available on request from website http://www.tropmet.res.in/~caipeex/. This work is part of PhD thesis of the first author. Authors acknowledge the contribution from several IITM scientists for the successful CAIPEEX project and the Director, IITM for the encouragement in carrying out this work. NCAR is supported by the Ministry of Earth Sciences (MoES), Govt. of India. W.W.G. acknowledges IITM financial support and hospitality during his visits to IITM. Authors are thankful to J-L. Brenguier, Meteo France, and G. Pandithurai, IITM, for providing valuable suggestions during early part of this work.

References

Andrejczuk, M., W. W. Grabowski, S. P. Malinowski, and P. K. Smolarkiewicz (2009), Numerical simulation of cloud-clear air interfacial mixing: Homogeneous versus inhomogeneous mixing, *J. Atmos. Sci.*, *66*, 2493–2500.

Baker, M. B., R. G. Corbin, and J. Latham (1980), The influence of entrainment on the evolution of cloud drop spectra: I. A model of inhomogeneous mixing, *Q. J. R. Meteorol. Soc.*, *106*, 581–598.

Baker, M. B., R. E. Breidenthal, T. W. Choularton, and J. Latham (1984), The effects of turbulent mixing in clouds, *J. Atmos. Sci.*, *41*, 299–304.

Bera, S., G. Pandithurai, and T. V. Prabha (2016), Entrainment and droplet spectral characteristics in convective clouds during transition to monsoon, *Atmos. Sci. Lett.*, *17*, 286–293, doi:10.1002/asl.657.
Blyth, A. M., W. A. Cooper, and J. B. Jensen (1988), A study of the source of entrained air in Montana cumuli, *J. Atmos. Sci.*, *45*, 3944–3964.
Böing, S. J., H. J. J. Jonker, W. A. Nawara, and A. P. Siebesma (2014), On the deceiving aspects of mixing diagrams of deep cumulus convection, *J. Atmos. Sci.*, *71*, 56–68.
Brenguier, J. L., and L. Chaumat (2001), Droplet spectra broadening in cumulus clouds. Part I: Broadening in adiabatic cores, *J. Atmos. Sci.*, *58*, 628–641.
Brenguier, J. L., and W. W. Grabowski (1993), Cumulus entrainment and cloud droplet spectra: A numerical model within a two-dimensional dynamical framework, *J. Atmos. Sci.*, *50*, 120–136.
Brenguier, J. L., H. Pawlowska, L. Schüller, R. Preusker, J. Fischer, and Y. Fouquart (2000), Radiative properties of boundary layer clouds: Droplet effective radius versus number concentration, *J. Atmos. Sci.*, *57*, 803–821.
Broadwell, J. E., and R. E. Breidenthal (1982), A simple model of mixing and chemical reaction in a turbulent shear layer, *J. Fluid Mech.*, *125*, 397–410.
Browning, K. A., and R. J. Gurney (1999), *Global Energy and Water Cycles*, Cambridge Univ. Press, Cambridge.
Burnet, F., and J. L. Brenguier (2007), Observational study of the entrainment-mixing process in warm convective clouds, *J. Atmos. Sci.*, *64*, 1995–2011.
Damiani, R., and G. Vali (2007), Evidence for tilted toroidal circulations in cumulus, *J. Atmos. Sci.*, *64*, 2045–2060.
Dimotakis, P. E. (2004), Turbulent mixing, *Annu. Rev. Fluid Mech.*, *37*, 329–356.
Freud, E., D. Rosenfeld, and J. R. Kulkarni (2011), Resolving both entrainment-mixing and number of activated CCN in deep convective clouds, *Atmos. Chem. Phys.*, *11*, 12,887–12,900.
Gerber, H., G. Frick, S. P. Malinowski, J.-L. Brenguier, and F. Burnet (2005), Holes and entrainment in stratocumulus, *J. Atmos. Sci.*, *62*, 443–459.
Gerber, H., G. Frick, J. Jensen, and J. Hudson (2008), Entrainment, mixing, and microphysics in trade-wind cumulus, *J. Meteorol. Soc. Jpn.*, *86A*, 87–106.
Grabowski, W. W. (1993), Cumulus entrainment, fine-scale mixing and buoyancy reversal, *Q. J. R. Meteorol. Soc.*, *119*, 935–946.
Grabowski, W. W. (2006), Indirect impact of atmospheric aerosols in idealized simulations of convective–radiative quasi equilibrium, *J. Clim.*, *19*, 4664–4682.
Grabowski, W. W., and T. L. Clark (1991), Cloud-environment interface instability: Rising thermal calculations in two spatial dimensions, *J. Atmos. Sci.*, *48*, 527–546.
Grabowski, W. W., and T. L. Clark (1993a), Cloud-environment interface instability, Part II: Extension to three spatial dimensions, *J. Atmos. Sci.*, *50*, 555–573.
Grabowski, W. W., and T. L. Clark (1993b), Cloud-environment interface instability, Part III: Direct influence of environmental shear, *J. Atmos. Sci.*, *50*, 3821–3828.
Grabowski, W. W., and H. Pawlowska (1993), Entrainment and mixing in clouds: The Paluch mixing diagram revisited, *J. Appl. Meteorol.*, *32*, 1767–1773.
Grabowski, W. W., and J. C. Petch (2009), Deep convective clouds, in *Clouds in the Perturbed Climate System: Their Relationship to Energy Balance, Atmospheric Dynamics, and Precipitation*, edited by J. Heintzenberg and R. J. Charlson, MIT Press, Cambridge, London.
Gray, W. M., and R. W. Jacobson (1977), Diurnal variation of deep cumulus convection, *Mon. Weather Rev.*, *105*, 1171–1188.
Heus, T. C., F. J. Pols, H. J. J. Jonker, H. E. A. van den Akker, and D. H. Lenschow (2009), Observational validation of the compensating mass flux through the shell around cumulus clouds, *Q. J. R. Meteorol. Soc.*, *135*, 101–112.
Jarecka, D., W. W. Grabowski, H. Morrison, and H. Pawlowska (2013), Homogeneity of subgrid-scale turbulent mixing in large eddy simulation of shallow convection, *J. Atmos. Sci.*, doi:10.1175/JAS-D-13-042.1.
Jeffery, C. A. (2007), Inhomogeneous mixing, invariance and Damköhler number, *J. Geophys. Res.*, *112*, D24S21, doi:10.1029/2007JD008789.
Jensen, J. B., and M. B. Baker (1989), A simple model of droplet spectral evolution during turbulent mixing, *J. Atmos. Sci.*, *46*, 2812–2829.
Jensen, J. B., P. H. Austin, M. B. Baker, and A. M. Blyth (1985), Turbulent mixing, spectral evolution and dynamics in a warm cumulus cloud, *J. Atmos. Sci.*, *42*, 173–192.
Khain, A., T. V. Prabha, N. Benmoshe, G. Pandithurai, and M. Ovchinnikov (2013), The mechanism of first raindrops formation in deep convective clouds, *J. Geophys. Res. Atmos.*, *118*, 9123–9140, doi:10.1002/jgrd.50641.
Klaassen, G. P., and T. L. Clark (1985), Dynamics of the cloud-environment interface and entrainment in small cumuli: Two-dimensional simulations in the absence of ambient shear, *J. Atmos. Sci.*, *42*, 2621–2642.
Konwar, M., R. S. Maheskumar, J. R. Kulkarni, E. Freud, B. N. Goswami, and D. Rosenfeld (2012), Aerosol control on depth of warm rain in convective clouds, *J. Geophys. Res.*, *117*, D13204, doi:10.1029/2012JD017585.
Korolev, A. V., and G. A. Isaac (2000), Drop growth due to high supersaturation caused by isobaric mixing, *J. Atmos. Sci.*, *57*, 1675–1685.
Krueger, S. (1993), Linear eddy modeling of entrainment and mixing in stratus clouds, *J. Atmos. Sci.*, *50*, 3078–3090.
Krueger, S. K., H. Schlueter, and P. Lehr (2008), Fine-scale modeling of entrainment and mixing of cloudy and clear air, *15th International Conference on Clouds and Precipitation*, Cancun, Mexico.
Krueger, S., C. W. Su, and P. McMurtry (1997), Modeling entrainment and fine scale mixing in cumulus clouds, *J. Atmos. Sci.*, *54*, 2697–2712.
Krueger, S., P. J. Lehr, and C. W. Su (2006), How entrainment and mixing scenarios affect droplet spectra in cumulus clouds, *Preprints, 12th Conf. on Cloud Physics, Madison, WI, Am. Meteorol. Soc.*, 9.2.
Kulkarni, J. R., et al. (2012), The Cloud Aerosol Interactions and Precipitation Enhancement Experiment (CAIPEEX): Overview and preliminary results, *Curr. Sci.*, *102*(3), 413–425.
Kumar, B., J. Schumacher, and R. A. Shaw (2012), Cloud microphysical effects of turbulent mixing and entrainment, *Theor. Comp. Fluid Dyn.*, 1–16, doi:10.1007/s00162-012-0272-z.
Lasher-Trapp, S. G., W. A. Cooper, and A. M. Blyth (2005), Broadening of droplet size distributions from entrainment and mixing in a cumulus cloud, *Q. J. R. Meteorol. Soc.*, *131*, 195–220.
Latham, J., and R. L. Reed (1977), Laboratory studies of the effects of mixing on the evolution of cloud droplet spectra, *Q. J. R. Meteorol. Soc.*, *103*, 297–306.
Lawson, R. P., and W. A. Cooper (1990), Performance of some airborne thermometers in clouds, *J. Atmos. Oceanic Technol.*, *7*, 480–494.
Lehmann, K., H. Siebert, and R. A. Shaw (2009), Homogeneous and inhomogeneous mixing in cumulus clouds: Dependence on local turbulence structure, *J. Atmos. Sci.*, *66*, 3641–3659.
Lu, C., Y. Liu, S. Niu, S. K. Krueger, and T. Wagner (2013), Exploring parameterization for turbulent entrainment-mixing processes in clouds, *J. Geophys. Res. Atmos.*, *118*, 185–194, doi:10.1029/2012JD018464.

Lu, C., Y. Liu, S. Niu, and S. Endo (2014), Scale dependence of entrainment-mixing mechanisms in cumulus clouds, *J. Geophys. Res. Atmos.*, *119*, 13,877–13,890, doi:10.1002/2014JD022265.

Malinowski, S. P., and H. Pawlowska (1989), On estimating the entrainment level in cumulus clouds, *J. Atmos. Sci.*, *46*, 2463–2465.

Norris, J. R. (1998), Low cloud type over the ocean from surface observations. Part II: Geographical and seasonal variations, *J. Clim.*, *11*, 383–403.

Paluch, I. R. (1979), The entrainment mechanism in Colorado cumuli, *J. Atmos. Sci.*, *36*, 2467–2478.

Paluch, I. R., and C. A. Knight (1984), Mixing and the evolution of cloud droplet size spectra in a vigorous continental cumulus, *J. Atmos. Sci.*, *41*, 1801–1815.

Paluch, I. R., and D. G. Baumgardner (1989), Entrainment and fine scale mixing in a continental convective cloud, *J. Atmos. Sci.*, *46*, 261–278.

Pawlowska, H., J. L. Brenguier, and F. Burnet (2000), Microphysical properties of stratocumulus clouds, *Atmos. Res.*, *55*, 15–33.

Prabha, T. V., A. Khain, R. S. Maheskumar, G. Pandithurai, J. R. Kulkarni, M. Konwar, and B. N. Goswami (2011), Microphysics of pre-monsoon and monsoon clouds, *J. Atmos. Sci.*, *68*, 1882–1901, doi:10.1175/2011JAS3707.1.

Prabha, T. V., S. Patade, G. Pandithurai, A. Khain, D. Axisa, P. Pradeep Kumar, R. S. Maheshkumar, J. R. Kulkarni, and B. N. Goswami (2012a), Spectral width of pre-monsoon and monsoon clouds over Indo-Gangetic valley, *J. Geophys. Res.*, *117*, D20205, doi:10.1029/2011JD016837.

Prabha, T. V., A. Khain, G. Pandithurai, J. Kulkarni, and B. N. Goswami (2012b), Vertical oscillations in monsoon clouds during CAIPEEX and the origin of small droplets, *16th International Commission on Clouds and Precipitation*, Leipzig, Germany, 30 July–4 Aug. 1059.

Pruppacher, H. R., and J. D. Klett (1997), *Microphysics of Clouds and Precipitation*, 2nd ed., 954 pp., Kluwer Acad.

Raga, G. R., J. B. Jensen, and M. B. Baker (1990), Characteristics of cumulus band clouds off the coast of Hawaii, *J. Atmos. Sci.*, *47*, 338–356.

Reuter, G. W., and M. K. Yau (1987), Mixing mechanisms in cumulus congestus clouds. Part I: Observations, *J. Atmos. Sci.*, *44*, 781–797.

Rogers, R. R., and M. K. Yau (1989), *A Short Course in Cloud Microphysics*, 3rd ed., 293 pp., Pergamon Press, Oxford.

Romps, D. M. (2016), The Stochastic Parcel Model: A deterministic parameterization of stochastically entraining convection, *J. Adv. Model. Earth Syst.*, *8*, 319–344, doi:10.1002/2015MS000537.

Scorer, R. S., and F. H. Ludlam (1953), Bubble theory of penetrative convection, *Q. J. R. Meteorol. Soc.*, *79*, 94–103.

Sherwood, S. C., P. Minnis, and M. McGill (2004), Deep convective cloud-top heights and their thermodynamic control during CRYSTAL-FACE, *J. Geophys. Res.*, *109*, D20119, doi:10.1029/2004JD004811.

Sherwood, S. C., S. Bony, and J.-L. Dufresne (2014), Spread in model climate sensitivity traced to atmospheric convective mixing, *Nature*, *505*, 37–42.

Slawinska, J., W. W. Grabowski, H. Pawlowska, and H. Morrison (2012), Droplet activation and mixing in large-eddy simulation of a shallow cumulus field, *J. Atmos. Sci.*, *69*, 444–462.

Squires, P. (1958) The microstructure and colloidal stability of warm clouds, *Tellus*, *10*, 256 − 261.

Stommel, H. (1947), Entrainment of air into a cumulus cloud, *J. Meteorol.*, *4*, 91–94.

Su, C. W., S. K. Krueger, P. A. McMurtry, and P. H. Austin (1998), Linear eddy modeling of droplet spectral evolution during entrainment and mixing in cumulus clouds, *Atmos. Res.*, *47–48*, 41–58.

Tölle, M. H., and S. K. Krueger (2014), Effects of entrainment and mixing on droplet size distributions in warm cumulus clouds, *J. Adv. Model. Earth Syst.*, *6*, 281–299, doi:10.1002/2012MS000209.

Warner, J. (1955), The water content of cumuliform clouds, *Tellus*, *7*, 449–457.

Warner, J. (1969), The microstructure of cumulus cloud. Part I. General features of the droplet spectrum, *J. Atmos. Sci.*, *26*, 1049–1059.

Warner, J. (1973), The microstructure of cumulus cloud: Part IV. The effect on the droplet spectrum of mixing between cloud and environment, *J. Atmos. Sci.*, *30*, 256–261.

Yum, S. S., and J. G. Hudson (2005), Adiabatic Predictions and observations of cloud droplet spectral broadness, *Atmos. Res.*, *73*, 203–223, doi:10.1016/j.atmosres.2004.10.006.

Yum, S. S., J. Wang, Y. Liu, G. Senum, S. Springston, R. McGraw, and J. M. Yeom (2015), Cloud microphysical relationships and their implication on entrainment and mixing mechanism for the stratocumulus clouds measured during the VOCALS project, *J. Geophys. Res. Atmos.*, *120*, 5047–5069, doi:10.1002/2014JD022802.